

“If you can't explain it simply, you don't understand it well enough.”

- Rutherford via Einstein

University of Alberta

**DEVELOPMENT OF A PROTOTYPE FOR A LOW DEAD TIME
DARK MATTER DETECTOR USING SUPERHEATED LIQUID**

by

Pitam Mitra

A thesis submitted to the Faculty of Graduate Studies and Research
in partial fulfillment of the requirements for the degree of

Master of Science

Department of Physics

©Pitam Mitra

Fall 2013

Edmonton, Alberta

Permission is hereby granted to the University of Alberta Libraries to reproduce single copies of this thesis and to lend or sell such copies for private, scholarly or scientific research purposes only. Where the thesis is converted to, or otherwise made available in digital form, the University of Alberta will advise potential users of the thesis of these terms.

The author reserves all other publication and other rights in association with the copyright in the thesis and, except as herein before provided, neither the thesis nor any substantial portion thereof may be printed or otherwise reproduced in any material form whatsoever without the author's prior written permission.

Abstract

PICASSO (Project in Canada to Search for Supersymmetric Objects) is a direct dark matter search experiment located at SNOLAB. PICASSO uses superheated Freon-10 (C_4F_{10}) as target for elastic scattering of Weakly Interacting Massive Particles (WIMPs) which are the most favored particle candidates for dark matter. In this thesis, a “geyser”, a small-scale working prototype of a low dead-time dark matter detector, is described. This detector has a novel design for the recovery of the active fluid. It is demonstrated that the detector can stably sustain superheated fluid for more than 48 hours.

Systematic studies have been performed of the stability, the dead time, energy thresholds and the operational parameters of the geyser. The geyser was operated stably for more than 73 hours, out of which 40 hours of thermodynamic, optical and acoustic data were analysed. An image analysis algorithm was developed to localize events. Acoustic data was analyzed using techniques from the PICASSO experiment. A strong discrimination effect between alpha-like events and nuclear recoil-like events was found .

Acknowledgments

First and foremost, I am indebted to my adviser Dr Carsten Krauss, for giving me the opportunity to work on a challenging, intellectually stimulating and exciting project. As an adviser, Carsten has always encouraged and supported me in my work and I am very grateful for his assistance and thoughtful guidance during my research work. As a scientist, he has been a great source of inspiration on my research. When he delivers a presentation or a lecture, he captures the attention of both experts and non-experts alike. Only a person with a very deep understanding of the subject can make it simple enough for everyone in the room. It is a very humbling experience to see him present something, be it in a colloquium or a public lecture. He is a great source of inspiration to me in my work and daily life.

I am immensely appreciative to Solange Gagnebin for her help and advice in every aspect of the project - from developing a cleaning mechanism, to the analysis. Solange always found time to discuss and help me with the problems, no matter how busy she was. I would like to thank Logan Sibley for his suggestions and constructive criticisms during my project.

I would like to thank the entire PICASSO collaboration for the discus-

sions which helped me a lot in this project.

Special mention goes to Jason Dibbs of the glass blowing shop. His expertise in glassblowing and his suggestions in the design were invaluable. My gratitude extends to Paul and Len of the electronics shop for helping me set up the electronics and the imaging.

I would like to thank the physics department at university of Alberta for providing me the opportunity and the environment for the research, and I would also like to thank the astro-particle group for their criticisms, comments, suggestions and help throughout the project. I would also like to acknowledge the support provided by my friends during my study. Thank you Dani for the “research” times as well.

No amount of thanks and gratitude would be enough to express the love and support that my family has given me unconditionally. To my mom and dad - the virtues that I claim today, are a result of your hard work and dedication in my upbringing, and the faults are mine alone.

Contents

1. Introduction	1
2. Dark Matter	4
2.1. Evidence for Existence	4
2.2. Nature of Dark Matter	8
2.3. Detection Methods	9
2.3.1. Direct Detection:	10
2.3.2. Indirect Detection:	10
2.3.3. Collider Production	11
3. Particle Detection with Superheated Liquids	12
3.1. Theory of Superheated Liquids and Bubble Nucleation	12
3.1.1. Energy Thresholds for Freon-10	17
3.2. Kinetics of Bubble Growth	18
3.2.1. Inertial Growth	19
3.2.2. Thermal Growth	20
3.2.3. Oscillations	22

3.3.	Signal Generation and Discrimination	22
3.3.1.	Alpha Neutron Discrimination	22
3.4.	The PICASSO Detectors	23
3.4.1.	Active Fluid, Gel Matrix and the TPCS	24
3.4.2.	Detector Response	25
3.5.	Location and Background	27
3.6.	PICASSO+ the Next Generation Detector	29
4.	The Geyser - Development and Technical Description	30
4.1.	Safety	31
4.1.1.	Chemical Safety	32
4.1.2.	Structural Safety	33
4.1.3.	Fire Safety	35
4.2.	Development of the Geyser	35
4.2.1.	The Geyser Prototype	36
4.3.	Bubble Lifecycle	42
4.4.	Quality Control	44
4.4.1.	Cleaning	45
4.4.2.	Filling and Degassing	45
4.5.	Electronic Control of the Geyser	46
5.	Operation and Data Sources	51
5.1.	Overview	51
5.1.1.	Acoustic Data Acquisition	51
5.1.2.	Pressure	55

5.1.3.	Temperature	56
5.1.4.	Optical Data Taking	58
5.2.	Data flow	59
5.2.1.	Hardware Server	60
5.2.2.	Geyser Control Algorithms	62
5.3.	Operation	62
5.3.1.	Start of Operation	62
5.3.2.	End of Operation	63
5.4.	Data quality:	64
5.4.1.	Correlation of Data Sources	64
5.4.2.	Stability of the Superheat	64
5.5.	Limitations of the Geyser.	65
6.	Analysis and Physics of the Geyser	68
6.1.	Event Localization	68
6.2.	PVar	75
6.3.	gFVar	79
6.4.	Expectation and Event Rates	83
6.4.1.	Determination of the Dead Time of the Geyser	86
6.4.2.	Track Length Effects and Efficiency	87
7.	Summary and Future Work	89
7.1.	Summary and Concluding Remarks	89
7.2.	Freon Based Geyser	90

7.3. Structural Changes	90
7.3.1. Scale of the Experiment	90
7.3.2. Geysers Material	91
7.3.3. Liquid Level Control	91
7.3.4. Retroreflectors and Diffuse Lighting	92
7.4. Data Acquisition Upgrade	92
Bibliography	93
A. Appendix	99
A.1. Runs Considered for Analysis	99
A.2. Contents of a .wfi file	100

List of Tables

3.1. Stages of bubble growth	23
4.1. Comparison of working conditions for the geyser with different fluids.	32
6.1. Activity in the geyser glass vessel produced from Thorium decay chain.	84
6.2. Activity in the geyser glass vessel from Uranium decay chain .	84
A.1. Runs considered for analysis	99

List of Figures

2.1.1.Expected and observed rotation curves	6
2.1.2.Composite image of MACS J0025.4-1222	7
3.1.1.Work as a function of bubble volume.	16
3.1.2.Energy threshold for recoils in ethanol	17
3.1.3.Calibration of PICASSO detectors with mono-energetic neutrons.	18
3.3.1.Time evolution of alpha vs F-recoil.	24
3.4.1.The PICASSO detector arrangement	25
3.4.2.Response of PICASSO detectors to different kinds of particles in superheated C_4F_{10}	26
3.5.1.Location of PICASSO in SNOLAB	27
3.5.2.Neutron flux due to cosmic rays as a function of depth in equiv- alent kilometres of water	28
4.0.1.A conceptual drawing of a large scale geyser.	31
4.1.1.Vapour pressure of ethanol	34
4.2.1.The geyser as built by Hahn and Reist	36
4.2.2.Geyser - Design and reverse thermal gradient.	37

4.2.3.Streaming and wall nucleation	42
4.3.1.Stages of bubble evolution.	44
4.5.1.Electronic control of the geyser	47
4.5.2.Electronic control circuit of the geyser.	48
4.5.3.Piezo-electric sensor circuit	49
5.1.1.Data acquisition and control system of the geyser	52
5.1.2.Acoustic data of an event from the geyser.	54
5.1.3.Average pressure changes in a bubble evolution. The dead time is driven by the trailing edge, and has been fitted with an ex- ponential decay with flat background.	57
5.1.4.Temperature variation during an event in top and bottom cool- ing chambers.	58
5.1.5.Camera image of the experiment. The region selected for the motion triggers is indicated by the rectangle.	59
5.2.1.Schematics of data flow of the geyser.	60
5.2.2.A schematic of the hardware interfacing program.	61
5.4.1.Average pressures runs considered for analysis.	65
5.4.2.Average temperatures in runs considered for analysis.	66
5.4.3.Average superheat achieved in the runs	67
6.1.1.The difference of frames when a nucleation occurs in (A) the main volume and (B) the mirror.	69
6.1.2.Frames before and during a bubble identification.	70
6.1.3.An event, after processing the image.	71

6.1.4.3D plot of event positions in the geyser.	73
6.1.5.Histogram of bubble radii.	74
6.1.6.3D map of neutron events localized inside the geyser and Monte- Carlo	75
6.1.7.Rates in equi-volume parts of the geyser	76
6.2.1.Superheat vs PVar of neutron runs	77
6.2.2.(Left) Pvar histogram of alpha and source runs. (Right) Nor- malized PVar histograms used for calculation of discrimination.	78
6.3.1.Average of scaled DFTs from source run events and alpha run events.	79
6.3.2.Superheat vs gFVar of neutron runs	80
6.3.3.The difference of average scaled DFTs between source run events and alpha run events	81
6.3.4.Average FFT spectrum of neutrons vs alpha runs	82
6.4.1.Sketch of the angle measurement for source position and effi- ciency calculation	86
6.4.2.Dead time measurements of runs at different temperatures . .	87
6.4.3.Distribution of the track length generated by a SRIM simulation of 10keV recoils in ethanol.	88

1. Introduction

One of the most intriguing puzzles in modern physics is that only 5% of the universe is made up of the forms of matter and energy that we know. Many astrophysical observations have confirmed that the majority of matter, which accounts for the gravitational interactions is unidentified. One mechanism to satisfy the astrophysical observations is to introduce dark matter consisting of cold, non-baryonic and neutral relic elementary particles better known as Weakly Interacting Massive Particles (WIMPs). These particles have a very low interaction cross section with ordinary matter, leading to nuclear recoils with a range of 100 keV in the target. Dark matter search is an active area of research today, with experiments around the world attempting to make a first detection of a WIMP signal. PICASSO (Project in Canada to Search for Supersymmetric Objects) is one such experiment, located at SNOLAB, near Sudbury, Ontario.

The PICASSO detectors use superheated liquid C_4F_{10} as the target for elastic scattering of WIMPs. Fluorine is expected to have an enhanced cross section to spin-dependent WIMP interactions which makes PICASSO primarily a spin dependent dark matter search experiment. Since the fluid is super-

heated a slight perturbation causes it to nucleate. When a particle interacts with the liquid in this meta-stable state, it causes nuclei to recoil that subsequently deposit energy along its track. This triggers the superheated fluid to undergo a phase change, and it boils. Piezoelectric sensors detect the acoustic signal that results from the rapid expansion of the resulting bubble, which then can be used to distinguish between alpha backgrounds and neutron or WIMP signals.

The superheated fluid only undergoes a phase change if the energy deposition from the recoil track is larger than a threshold energy. This causes the detector to be insensitive to low energy backgrounds such as gamma rays or electrons. The threshold energy can be controlled using pressure and temperature. The PICASSO detectors are contained within specially designed Temperature and Pressure Control Systems (TPCS) enabling operation at well defined thresholds.

In this thesis, a small scale working prototype of a low dead time “geyser” type detector will be described. This prototype is intended to be a basic scale model of future versions of PICASSO detectors (PICASSO+), which aim for large volume dark matter experiments of over 100 kg.

Chapter 2 discusses the known evidence indicating that our universe has excess matter, which has a gravitational potential, yet can’t be seen, and discusses possible candidates for the missing matter. Chapter 3 describes the theory of nucleation, and particle detection using superheated liquid. A discussion of the present PICASSO detectors, their construction, operation and backgrounds are also discussed. Chapter 4 describes the technical aspects of

the prototype detector, including the design elements, the scope and the geometry of the detector. Important safety features, data taking setup, quality control including cleaning and a filling and emptying procedure are also discussed in this chapter. Chapter 5 discusses the operation of the geysers, and the data acquisition.

Chapter 6 discusses the analysis of the stability of the geysers, selection of good runs for analysis, image analysis and analysis of the acoustic data from the geysers. Variables and analysis techniques used by the PICASSO collaboration and the analysis of the geysers data are described. Finally, a new variable, constructed and optimized for the analysis of the geysers is introduced. The conclusion and future scope of this work is presented in Chapter 7.

2. Dark Matter

The dark matter problem is one of the most fundamental and exciting open questions of physics. The first observations of the effects of dark matter came in early 1920, from measurements of motion of stars near the galactic plane [1] implying the gravitational influence of an undisclosed component of mass. In 1933 Fritz Zwicky came to the same conclusion from observing the dynamics of the Coma cluster [2]. He conferred this missing mass the name “dunkle (kalte) Materie” meaning “dark (cold) matter”.

2.1. Evidence for Existence

Today, there is an abundance of evidence for dark matter from astronomy and cosmology. Observations in the past 30 years, significant effort has gone into understanding what dark matter is, and many theories have been developed in an attempt to explain the missing matter. Astrophysical observations of galactic rotation curves and “maps” of the mass distribution in the universe using gravitational lensing have been constructed [3]. Observations of anisotropies of the Cosmic Microwave Background (CMB) have also put a constraint on

the dark matter density of the universe [4]. All these different observations can consistently be explained by the existence of dark matter. A few examples showing the evidence of dark matter have been selected from a large range of fields such as observational astrophysics, microwave astronomy to big bang nucleosynthesis and have been summarized below. A majority of the evidence is taken from the framework of the Λ -CDM (Cold Dark Matter) model [5], also referred to as the benchmark model of cosmology. In this model, dark matter (CDM) is taken to be non-relativistic, non baryonic and to have a very weak self interaction.

Rotation Curves: The orbital velocity of stars in a galaxy can be plotted vs the distance to the center of the galaxy. In Figure 2.1.1, the expected rotation curve and the observed rotation curves are shown for a few galaxies. The rotation curves indicate that an excess of mass is present than optically observed.

Mass to luminosity ratio: The mass to luminosity ratios of different structures in the universe can be compared. The structures observed in the universe show a high mass to luminosity ratio, indicating the presence of dark matter [8].

Weak field lensing of colliding galaxy clusters: The bullet cluster (1E 0657-558) and MACS J0025.4-1222 (Figure 2.1.2) are two pairs of galaxy clusters which have collided in the past. Studies with gravitational lensing and X-ray images show that the majority of the hydrogen is within the region near the centre of the clusters while the majority of the mass is distributed near the edges. The explanation for this distribution is that the dark matter

2.1 Evidence for Existence

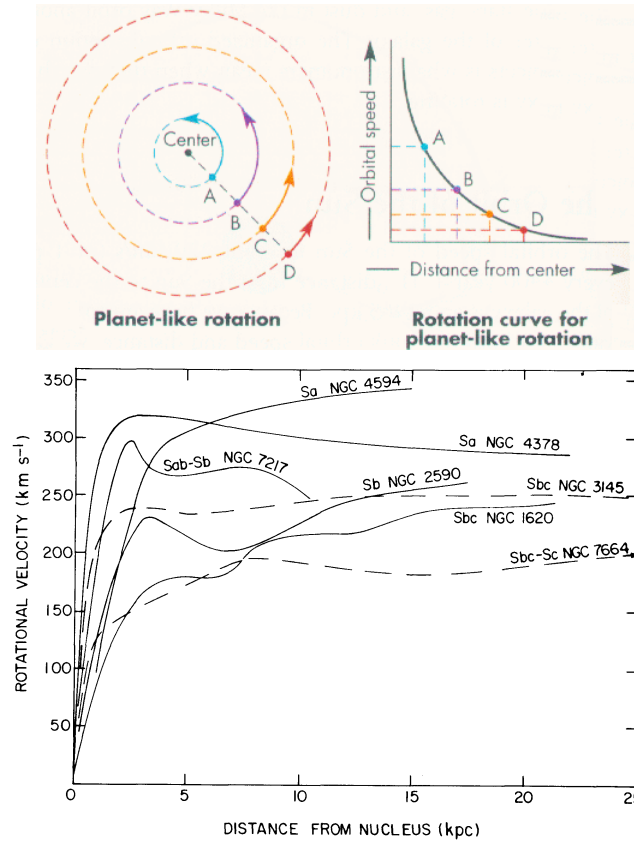


Figure 2.1.1.: Expected Rotation curve for a galaxy or a planetary system (top) and Observed Rotation curve for several galaxies. (bottom) [6, 7]

component traversed the interaction unhindered, while the baryonic component experienced drag. Thus the two centers of mass of the galaxy clusters (shown as the red outer contours in Figure 2.1.2) have outpaced the visible x-ray emitting components (shown as the yellow centre contours). The spatial offset of the center of total mass from the center of the baryonic mass peaks cannot be explained by modified gravity theories like MOND [9] and TeVeS [10]. The evidence here also supports the expectation that dark matter particles interact weakly.

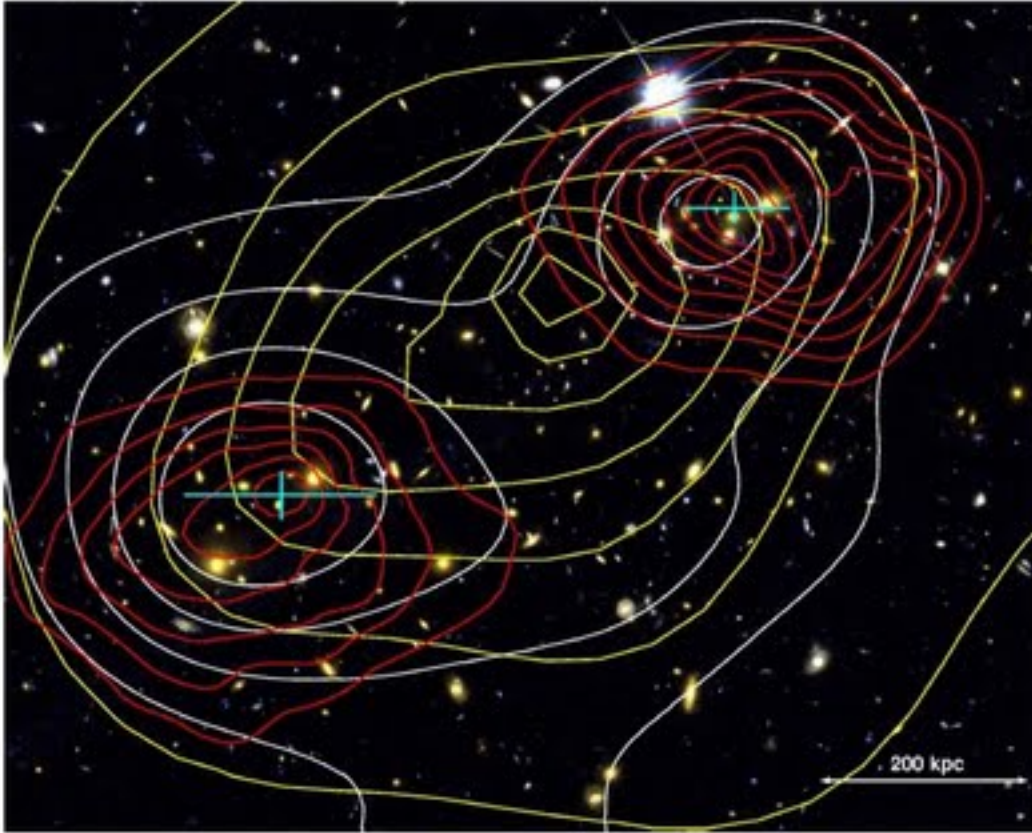


Figure 2.1.2.: Composite image of MACS J0025.4-1222, made from separate exposures of Hubble space Telescope and Chandra X-Ray Telescope [11].

Cosmic Microwave Background (CMB) power spectrum: The ratio of baryon abundance to dark matter influences the CMB power spectrum. The series of 3rd or higher acoustic peaks in the CMB power spectrum is sensitive to the energy density ratio of dark matter to radiation in the universe. The amount of radiation can be inferred from the measured temperature of the CMB and the thermal history. Fitting the 3rd peak to the Λ -CDM model of the universe gives the dark matter density [12]. This is important because this measurement is independent of all other astronomical observations and

confirms the existence of dark matter, and the density of dark matter measured from the CMB agrees with the value calculated from measurements of structure formation in the universe. [12]

2.2. Nature of Dark Matter

The nature of dark matter is yet to be understood. A number of basic properties of dark matter particles have been determined from observations, a summary of which is given below:

Dark matter is non-baryonic in nature. The density parameter, Ω , is defined as the ratio of the observed density to the critical density of the universe. The density parameter of dark matter in the universe has been found to be 0.222 ± 0.026 [4]. However, the density parameter of baryonic matter is 0.0449 ± 0.0028 [4]. This indicates that dark matter is non-baryonic in nature.

Dark matter is electromagnetically neutral and it should not have coupled strongly with photons during the recombination period, which places limits on the interaction of dark matter with photons. This constraint yields a limit on the dipole moment of dark matter particles, $[D, M] < 3 \times 10^{-16} \text{e cm}$ for masses less than a few GeV and $[D, M] < 10^{-24} \text{e cm}$ for larger masses where D is the electric dipole moment and M is the magnetic dipole moment [13].

Dark matter is “cold” or slow moving. N-body simulations show that the radial velocity distribution of dark matter particles in the galaxy follows a

generalized gaussian with a mean velocity of 224 km/s and the tangential velocity follows a double gaussian with the mean at 0 and 150 km/s respectively. [14]

Dark matter interacts “weakly”. A requirement of dark matter particles is that they do not couple strongly with baryonic particles during the recombination period after the big bang. This would be inconsistent with the observed peaks in the CMB power spectrum. If the coupling is strong, then the baryon-dark matter fluid would radiatively cool, affecting structure formation. Many theories beyond the standard model predict WIMPs as possible dark matter candidates that weakly couple to gauge bosons. WIMPs, if produced thermally in the early universe would have resulted in an abundance which is consistent with the dark matter abundance today, and hence they are the most studied class of dark matter candidates.

Dark matter is stable. The dark matter, if produced in the early universe, must be stable on cosmological time scales otherwise it would have affected the CMB anisotropies during the recombination epoch and the large scale structures today. Theories predicting multiple dark matter particles decaying into the lightest dark matter particle are severely constrained by the requirement that such a decay may not disrupt the dark matter structure formation. [15]

2.3. Detection Methods

Astrophysical observations permit estimates of large scale quantities of dark matter, including its density, but do not allow one to determine its particle

properties. For this purpose some other method involving direct interactions and direct signals is required. Detection methods for dark matter can be broadly classified into 3 categories: direct detection, indirect detection and collider production.

2.3.1. Direct Detection:

In this method, detectors are designed to directly detect the local dark matter particles by scattering off ordinary nuclei to produce either acoustic signals (PICASSO, COUPP) or charged particle avalanches (DMTPC) or scintillation (XENON and DEAP). Present experiments are setting limits on the cross section of interaction of dark matter particles.

2.3.2. Indirect Detection:

Dark matter particles may annihilate or decay to produce standard model particles like photons and neutrinos. Some experiments (IceCUBE, ANTARES) use Cerenkov light from secondaries of high energy neutrinos to detect an annihilation signal. Another possible signal of dark matter annihilation could be observed with gamma ray photons originating in regions of astrophysical concentrations of dark matter such as galaxy clusters or centers of galaxies. Such measurements are expected to yield dark matter mass and annihilation cross sections of WIMPs if evidence of dark matter annihilation could be established.

2.3.3. Collider Production

Particle colliders like the LHC, aim to reproduce conditions prevailing in the early universe via high energy collisions. It is expected that such collisions may create dark matter particles. Colliders can provide us with information on production rates, interaction cross sections and other particles produced, if any, in such interactions.

Any single method of dark matter detection will not be enough to confirm the properties of the cosmological dark matter particle, and verification will be needed from astrophysical observations to support such a claim.

3. Particle Detection with Superheated Liquids

In a bubble detector, droplets of a superheated fluid like Freon-10 (C_4F_{10}) are suspended in a gel matrix. When a particle deposits energy in the superheated liquid, the droplet undergoes a phase transition to the gaseous state. The expansion of the droplet happens fast and the volume of the droplet changes by about ~ 150 times based on the density of liquid and gaseous Freon-10. This rapid expansion causes acoustic pressure waves, which are transmitted through the detector and are picked up by piezo-electric sensors. The sensors produce a voltage, which is then digitized and recorded.

3.1. Theory of Superheated Liquids and Bubble Nucleation

The nucleation of superheated liquids has been demonstrated as an early means for particle detection. The theory of the behavior of superheated liquids was

3.1 Theory of Superheated Liquids and Bubble Nucleation

described for bubble chambers by F. Seitz, Milton S. Plesset, Stanley Alan Zwick and Paul Dergarabedian [16, 17, 18]. There are two different limits for superheating a fluid. The first is called the thermodynamic limit of superheat that defines a phase boundary which separates meta-stable states from thermodynamically unstable states. The physical reason behind this limit is that the entropy in this phase boundary is at its maximum, and hence entropy production has reached zero. This phase boundary is asymptotic. Above this limit a superheated fluid ceases to exist in a liquid state. The thermodynamic limit of superheat is important because the definition of reduced superheat, as used by PICASSO [19], depends on this limit. Using the Val-der-Waal’s equation of state $(P + \frac{n^2a}{V^2})(V - nb) = nRT$, this limit for an organic compound gives $T_{therm} = 0.844T_c$ where T_c is the critical temperature [20].

The second limit is the kinetic limit of superheat. This limit is imposed by bubble nucleation probability. As the temperature of a liquid rises or the pressure falls, the probability of a nucleation increases. Eventually, the “mean wait time” for such a bubble becomes short, and it becomes difficult to achieve higher temperatures [21].

A nucleation bubble has a defined life-cycle. Initially a protobubble is created where a free gas cavity is created that requires an energy equal to σA , where σ is the surface tension and A is the surface area of the cavity. Work is done by gas molecules entering the cavity. Nucleation theory requires this process to be isothermal and reversible [20]. The amount of work done by the molecules entering the protobubble and expanding at a constant pressure is given by $P\Delta V$, where P is the pressure and ΔV is the change in volume. If x

3.1 Theory of Superheated Liquids and Bubble Nucleation

molecules are vaporized at a constant pressure, P_V , into a constant area submerged in a liquid with pressure P_L , and kept under an external counterforce per unit area $P_V - P_L$, then the work done by the gas on the environment is given by:

$$W_1 = (P_V - P_L)V_G' \quad (3.1.1)$$

Here V_G' is the volume inside the membrane enclosing the x molecules at pressure P_V . If the gas volume is then expanded from V_G' to V_G , while keeping the number of molecules constant, the work done on the environment is given by:

$$W_2 = \int_{V_G'}^{V_G} (P - P_L)dV = P_G V_G - P_V V_G' - P_L(V_G - V_G') - \int_{P_V}^{P_G} V dP$$

here P is the pressure inside the cavity during the volume change. Simplifying further

$$W_2 = P_G V_G - P_V V_G' - P_L(V_G - V_G') - x(\mu_G - \mu_L)$$

where μ is the chemical potential defined by $d\mu = \frac{V}{x}dP$. Therefore, the minimum amount of work needed to form a bubble assuming that the total volume of the system is constant, is given by:

$$W = \sigma A - W_1 - W_2$$

or

$$W = \sigma A - (P_G - P_L)V_G + x(\mu_G - \mu_L) \quad (3.1.2)$$

Equation 3.1.2 is known as the fundamental equation of bubble nucleation [20], from which one may infer there is a minimum amount of energy required to nucleate a superheated liquid. This is an advantage for detectors using superheated fluids especially for dark matter searches where operation insensitive to minimally ionizing particles provides low backgrounds. Work required to create a bubble first increases, and then reaches a maximum since as a bubble is forming the vapour pressure must overcome the surface tension and the chemical potential. Once the equilibrium is reached the energy requirement is reduced and the energy is ultimately released. A plot of the work vs the average protobubble radius is shown in Figure 3.1.1 [20, 22]. A protobubble with a radius smaller than the equilibrium radius will collapse back into the liquid while a larger radius protobubble will expand.

Bubbles with critical volume have a critical radius, r_c , identified as the maximum of the work with respect to radius. Evaluating the derivative of W with respect to r and setting it to 0, the term with the chemical potential is removed. Setting $P_G = P_V$ Equation 3.1.2 simplifies to the Laplace – Kelvin Equation :

$$P_V - P_L = \frac{2\sigma}{r_c} \quad (3.1.3)$$

This can be used to calculate the critical radius of the bubble r_c . In most

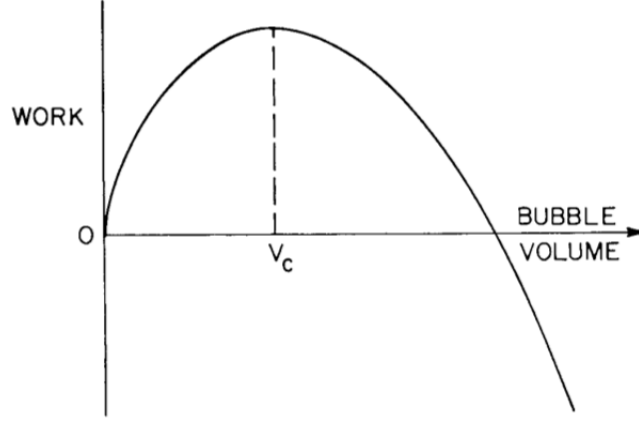


Figure 3.1.1.: Work as a function of bubble volume. V_C labels the point of the critical volume. [20, 22]

superheated fluids, P_L is much smaller than P_V and hence the former term can be ignored.

The minimum energy needed to form a bubble greater than or equal to the critical radius and equilibrium vapour pressure is given by [16]:

$$E = 4\pi\sigma R^2 + \frac{4\pi}{3}R^3 nH \quad (3.1.4)$$

where n is the number of moles of gas in the protobubble, H is the latent heat of sublimation per mole and R is the gas constant. This energy cannot be provided by the liquid, and must come from other sources of nucleation like particle interactions. Equation 3.1.4 can be further simplified to :

$$E = 16\pi \frac{\sigma^3}{P^2} \left(1 + \frac{2H}{3ZRT}\right) \quad (3.1.5)$$

where Z is the compressibility factor. The threshold energy of a fluid may

3.1 Theory of Superheated Liquids and Bubble Nucleation

be calculated from this equation and Figure 3.1.2 shows the threshold energy from Equation 3.1.5 for Ethanol.

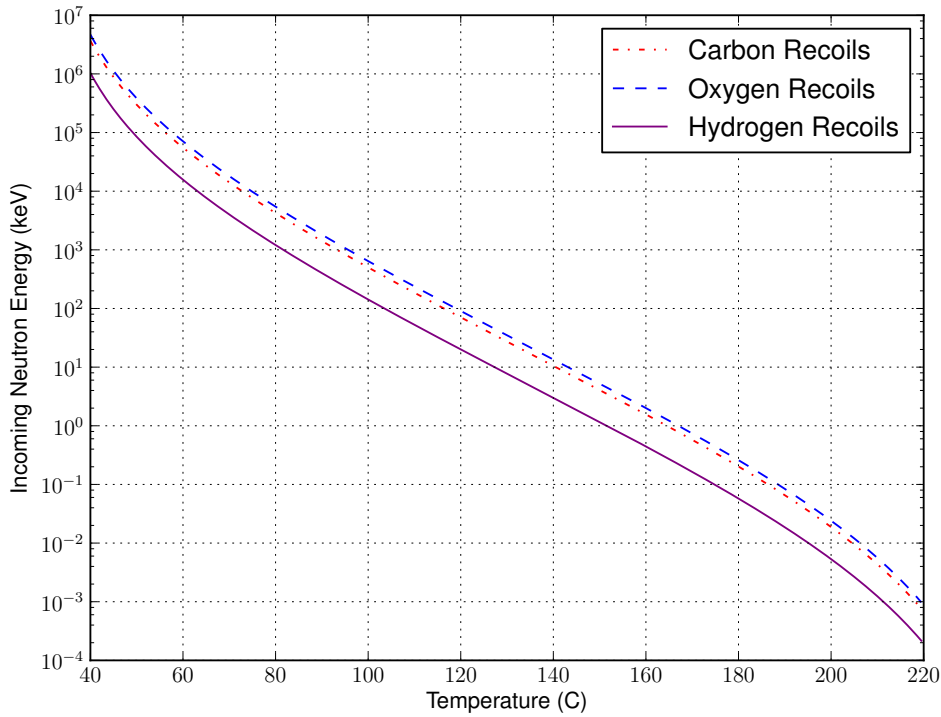


Figure 3.1.2.: Energy threshold for hydrogen, oxygen and carbon recoils in ethanol as a function of temperature assuming that the ambient pressure is 0.1055 bar.

3.1.1. Energy Thresholds for Freon-10

The PICASSO collaboration has measured the threshold energy vs temperature in Freon-10 using a mono energetic neutron beam at the University of Montreal tandem accelerator facility. The results are summarized in Figure 3.1.3. PICASSO is the only spin dependent dark matter search to calibrate the de-

3.2 Kinetics of Bubble Growth

tectors to 0.8 keV! The consistency between the model from Equation 3.1.5 and the data suggests that Ethanol would have a threshold between 50 keV and 300 keV.

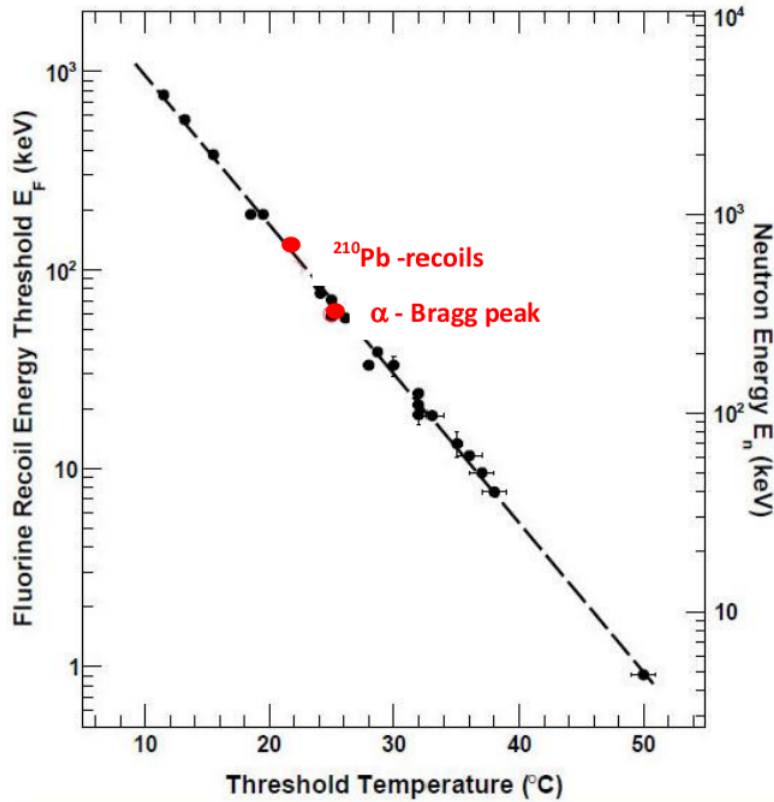


Figure 3.1.3.: Calibration of PICASSO detectors with mono-energetic neutrons on ^{19}F , with 146 keV ^{210}Pb recoil nuclei and 60 keV energy depositions from alpha particles at their Bragg peak are also shown. The calibration extends from 0.8 keV to 800 keV. [23]

3.2. Kinetics of Bubble Growth

Bubble growth, following formation of the proto-bubble occurs in two stages:

1. Inertial growth (sometimes referred to as Rayleigh growth) which is controlled by the energy stored in the bubble due to vapour pressure and by surface tension.
2. Thermal growth which is controlled by heat transfer from the fluid.

Note that the radius of the initial protobubble does not affect the later stages. Each type of growth is described in the following section.

3.2.1. Inertial Growth

Since the protobubble is formed in an unstable equilibrium, it expands. The first growth that results is the inertial growth due to the contents of the bubble being at a very high pressure (vapour pressure), compared to the surroundings. An upper bound for this growth rate is given by [24]:

$$\left(\frac{dR}{dt}\right)_{inertial} = \left[\frac{2p_v(T)-p}{2\rho}\right]^{1/2} \quad (3.2.1)$$

where R is the bubble radius at time t , ρ is the liquid density, $p_v(T)$ is the vapour pressure of the liquid as a function of temperature and p is the pressure of the liquid at the depth where the bubble is formed. As the bubble expands, the pressure inside decreases. This expansion is adiabatic and the vapour contents of the bubble cool. The inertial expansion rate slows and eventually becomes negligible compared to the bubble size. Thermal expansion (explained in 3.2.2) then drives any further expansion. The time for this inertial growth is on the order of a few tens of microseconds.

Equation 3.2.1 can be rewritten as:

$$\frac{dR}{dt} = \Phi_1 \quad (3.2.2)$$

where Φ_1 is a constant. For C_4F_{10} , $\Phi_1 = 1.2m/s$.

The intensity of sound emitted from the bubble growing in the fluid is [25]:

$$I = \frac{\rho \ddot{V}^2}{4\pi c} \quad (3.2.3)$$

where ρ is the density of fluid and c is the speed of sound and V is the volume of the bubble. Assuming a spherical bubble:

$$I_R = \frac{16\pi\rho\Phi_1^6}{c}t^2 \quad (3.2.4)$$

The intensity increases with temperature in the inertial growth as shown in Equation 3.2.4.

3.2.2. Thermal Growth

The driving factor following the initial kinetic expansion is the heat flowing into the bubble, and the expansion at this point becomes isothermal. That is, the temperature remains constant, and the heat flow into the bubble through the bubble surface membrane provides the energy for the expansion of the gas.

3.2 Kinetics of Bubble Growth

The rate of change of bubble radius in this phase is given by [24]:

$$\left(\frac{dR}{dt}\right)_{thermal} = \left(\frac{3}{\pi}\right)^{\frac{1}{2}} \frac{k}{L\rho_v} \frac{T - T_b}{(Dt)^{\frac{1}{2}}} \quad (3.2.5)$$

where k is the liquid thermal conductivity, L is the latent heat, and D is thermal diffusivity, T is the temperature and T_b is the boiling point. Equation 3.2.5 can be rewritten as:

$$\frac{dR}{dt} = \frac{\Phi_2}{2} \frac{1}{\sqrt{t}} \quad (3.2.6)$$

For C_4F_{10} , $\Phi_2 = 4.2\text{m}/\sqrt{s}$, and the intensity of sound emitted in the fluid is given by [25]:

$$I_T = \frac{16\pi\rho\Phi_2^6}{4c} \frac{1}{t} \quad (3.2.7)$$

The intensity decreases with time as shown in 3.2.7.

Hence, in the life cycle of a bubble, the intensity first increases during inertial growth and then decreases during thermal growth. The time required for the inertial growth to evolve into thermal growth is given by:

$$\tau = \left(\frac{\Phi_2}{\Phi_1}\right)^2 \quad (3.2.8)$$

where τ ranges from 140 - 500 μs in the operating temperature range for PICASSO detectors (20° C - 50° C) assuming C_4F_{10} . The signal emission of PICASSO lies in the inertial growth phase of the bubble.

3.2.3. Oscillations

Once the thermal growth stage is complete, the bubble undergoes a final phase where it freely oscillates harmonically, with a resonant frequency (Minnaert frequency), given by [26]:

$$\nu_R = \frac{1}{2\pi R_b} \sqrt{\frac{3kP_\infty}{\rho_l}} \quad (3.2.9)$$

where k is the polytropic index, ρ_l is the density of the liquid, P_∞ is the pressure of the fluid far from the bubble and R_b is the radius of the bubble.

3.3. Signal Generation and Discrimination

Table 3.1 summarizes the growth of a bubble in 5 stages. The region of interest for PICASSO lies in stage 4 (“Growth of the proto bubble past the critical radius”) as discussed in section 3.2.

3.3.1. Alpha Neutron Discrimination

Nuclear recoils and α particles have very different energy loss resulting in a difference in track length. This causes a subtle but distinguishable difference in the nucleation of a superheated liquid between alpha induced and recoil induced bubbles. Figure 3.3.1 illustrates the time evolution of an alpha vs a fluorine-recoil event. A time scale can be defined by $t_\alpha = \frac{L_\alpha}{\Phi_1} = 30\mu s$. A discrimination is expected at $t < 100\mu s$, in the acoustic data. The PICASSO

3.4 The PICASSO Detectors

Stage	Development	Remarks
Stage 1: $t = 10^{-16}$ s	Interaction of charged particle, energy transfer to electrons	
Stage2: $t = 10^{-13}$ s	Transfer of energy from electrons to kinetic energy of atoms, heating around track, electro-acoustical effect	UHE ν -physics: Antares, IceCube
Stage 3: $t =$ $10^{-10} - 10^{-9}$ s	Emergence of gas phase in nucleation region 10^{-9} to 10^{-8} m	Acoustic emission: Protobubble
Stage 4: $t > 10^{-9}$ s	Growth of proto-bubble once $R > r_c$. Inertial Growth	Increasing acoustic emission. Region of interest for recoil vs alpha discrimination for PICASSO.
Stage 4: $t > 10^{-4}$ s	Thermal Growth	Decreasing acoustic emission
Stage 5: $t > 10^{-3}$ s	Oscillations of free bubble	

Table 3.1.: Stages of bubble growth

collaboration has shown that such a discrimination exists in the frequency ranges between 20 kHz to 120 kHz.

3.4. The PICASSO Detectors

The PICASSO detectors consist primarily of droplets of active liquid suspended in a gel matrix contained within a cylindrical acrylic container. Piezoelectric sensors and temperature monitoring equipment are mounted on the container. A schematic of the arrangement is shown in Figure 3.4.1.

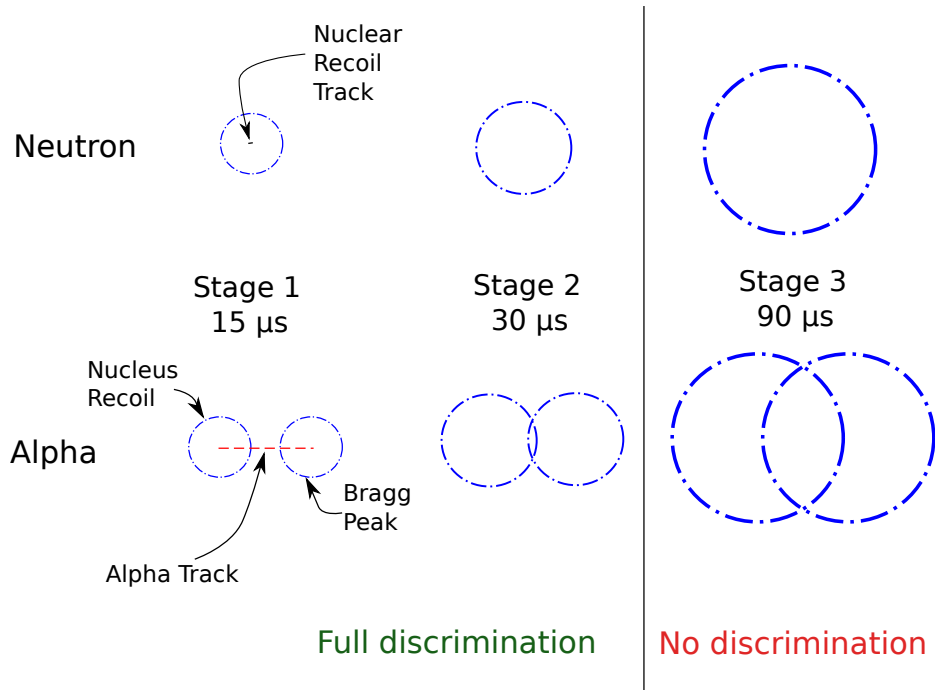


Figure 3.3.1.: Time evolution of alpha vs F-recoil. In an alpha event, the track length is longer and multiple protobubbles can be formed which converge into a larger bubble. In a recoil, a single protobubble is formed.

3.4.1. Active Fluid, Gel Matrix and the TPCS

The active liquid in a PICASSO detector is Freon-10 (C_4F_{10}). The boiling point of the fluid is $-1.7^\circ C$ while the detectors are operated between $30-50^\circ C$. Four detectors are placed inside a box, called “Temperature and Pressure Control System” (TPCS). Each TPCS measures 65 cm x 65 cm x 63 cm. Additionally, the TPCSs are insulated by a 1” layer of PVC foam. The top and the bottom plate of the TPCS are heated using eight 25Ω resistors, which provide a uniform temperature profile.

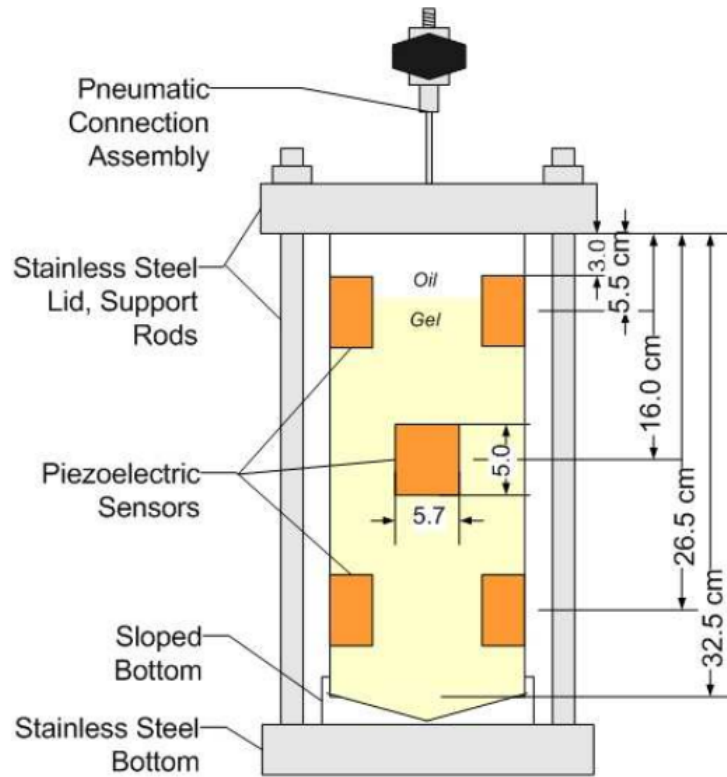


Figure 3.4.1.: The PICASSO detector schematic [27]

3.4.2. Detector Response

Figure 3.4.2 shows PICASSO's response curve with respect to particles of different energies. The first series from the right is ^{210}Pb recoils at 500 keV from ^{226}Ra . The detector's response increases sharply with increasing temperature and then reaches a plateau. At higher energies, the dash-dotted represents neutron recoils from a poly-energetic AcBe source. The line to the left is the expected response for a 50 GeV WIMP and the line to the far left with squares is from 1.75 MeV γ rays. Since the detector becomes sensitive to alphas before nuclear recoil like events, it is necessary to discriminate between the two types

of events. This is important since WIMP events are expected to behave like neutrons. Low specific energy loss particles like electrons, muons and γ rays become detectable at temperatures > 50 °C. This is much higher than the regular operational temperature for WIMP searches and thus the PICASSO detectors are largely insensitive to backgrounds from these events. The alpha and neutron events may be discriminated using the acoustic discrimination identified in 2006 [28].

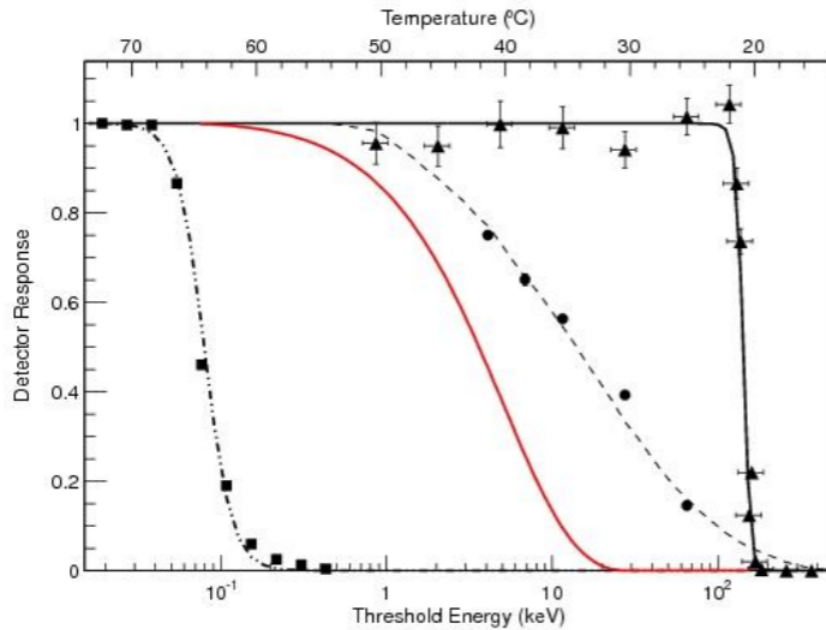


Figure 3.4.2.: Detector response to different kinds of particles in superheated C_4F_{10} . From left to right: response to 1.75 MeV γ -rays and minimum ionising particles (dash-dotted); ^{19}F recoils following scattering of a 50 GeV/c^2 WIMP; poly-energetic neutrons from an AcBe source (dotted); ^{210}Pb recoil nuclei from ^{226}Ra spikes (solid).

3.5. Location and Background

The PICASSO experiment has 32 detectors in operation at SNOLAB, which is an underground laboratory situated 2 km deep in a nickel mine in Sudbury, Ontario. A map of SNOLAB with the location of PICASSO is given in Figure 3.5.1.

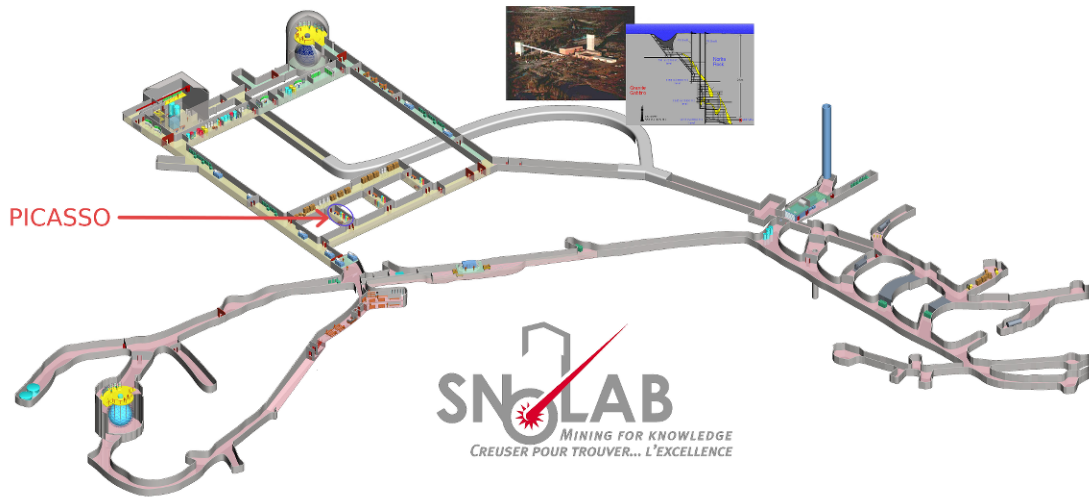


Figure 3.5.1.: Location of PICASSO in SNOLAB

Background mitigation is key in a rare event experiment like PICASSO. In this detector neutrons may produce signals that mimic those expected for WIMPs, and hence reduction of the neutron background is important. Cosmic ray showers produce muons which may interact with materials around the detectors and produce spallation. Therefore, reducing the atmospheric muon flux, and thus the neutron flux, is essential. For this reason PICASSO is located at SNOLAB, which is in a Vale Ltd. Nickel mine, 2070 m be-

3.5 Location and Background

low the surface of the earth. With 6010 m water equivalent of shielding the muon flux is reduced to $0.27 / (m^2 \cdot \text{day})$ resulting in a thermal neutron flux of $4144.9 \pm 49.8 \pm 105.3$ neutrons/ $(m^2 \cdot \text{day})$ and a fast neutron flux of approximately 4000 neutrons/ $(m^2 \cdot \text{day})$. [29]. A graph showing the background neutron flux due to cosmic rays in different sites around the world, in comparison to SNOLAB is shown in Figure 3.5.2.

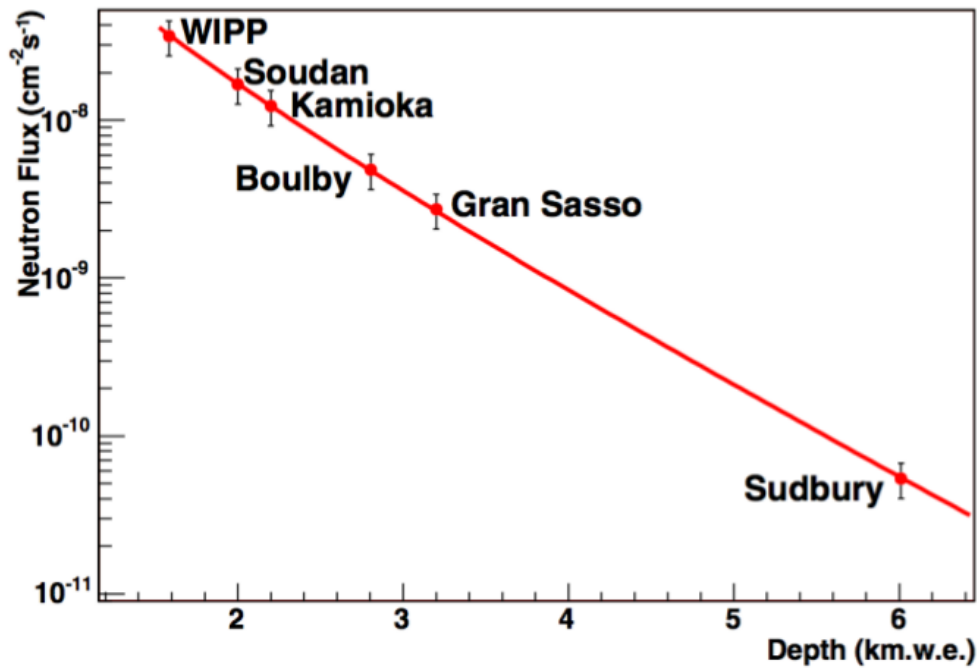


Figure 3.5.2.: Neutron flux due to cosmic rays as a function of depth in equivalent kilometres of water [30]

3.6. PICASSO+ the Next Generation Detector

The PICASSO collaboration has proposed to build a new type of detector in the future, which will allow the experiment to be scaled up to 500 kg with Freon as active mass. The new detectors will be a variant of a bubble chamber technique known as a geyser, suitable for an experiment with low count rates. The goals for such a detector include:

1. The system is safe.
2. The system is self-regulating. The nucleation bubbles formed will rise, and then be cooled down by a condenser with the fluid subsequently returning to the active volume without recompression.
3. The system is scalable to a large active mass.
4. The background level is reduced from $1/(\text{kg day})$ in current detectors to $10^{-6}/(\text{kg day})$, thus increasing the detector's sensitivity to WIMPs of cross sections of 10^{-7} pb from a current 10^{-2} pb level.
5. The system has a low dead time, and can run continuously without the need for external intervention.

4. The Geyser - Development and Technical Description

The PICASSO collaboration presently uses superheated droplet detectors to search for Dark Matter. To significantly scale up the experiment, a new type of detector is needed. A variant of the bubble chamber, with a condenser on the top known as a geyser type detector has been proposed for this. With simple operation and no moving parts, the main volume of target liquid is kept at constant superheat while the liquid in the neck of the detector is actively cooled. Nucleation bubbles rise to the cooler part of the detector, condense and then fall back to the active volume. A conceptual drawing of such a detector is shown in Figure 4.0.1.

To design such a detector, a study of properties of suitable fluids was performed. A summary is given in Table 4.1 [24]. Ethanol was selected given it is economically feasible for the early stages of development and can be operated at moderate temperatures. In later stages it is assumed that the fluid would be replaced by C_4F_{10} .

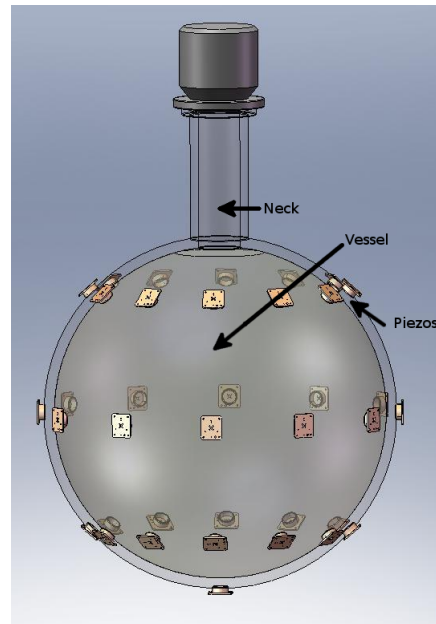


Figure 4.0.1.: A conceptual drawing of a large scale geysir. The spherical volume contains the active liquid, onto which a condensing neck has been mounted. Bubbles formed in the active volume rise through the neck and are cooled. [31]

4.1. Safety

As indicated in chapter 3, safety is a primary concern for a large volume superheated detector. The various aspects of the safety of the operation of a geysir include:

1. Chemical safety: safety in handling the chemicals required for cleaning the geysir and procedure for handling the active fluid
2. Structural safety: the safety of the geysir's structure, with respect to the pressures within it.
3. Fire safety: safety measures to prevent a fire, since the active liquid is

	Water	C_4F_{10}	Ar	Ethanol
Available Purity	High	Usually 99%.	~100%	~100%
Cost	Low	Moderate	Low	Low
Operating Temperature	230 °C	50°C	-160 °C	110 °C
Spin Coupling	Yes (P)	Yes (P)	No	Yes (P)
Max operational pressure	20 atm	5 atm	13 atm	6 atm
Max Bubble Size (a function of the top and bottom temperatures)	6 mm Top: 250°C Bottom: 100°C	1.2 cm Top: 29°C Bottom: 0°C	6 mm Top: -270°C Bottom: -260°C	1 cm Top: 110°C Bottom: 30°C

Table 4.1.: Comparison of working conditions for the geyser with different fluids. The bubble size was calculated by taking into account the superheat given by the difference of the boiling point due to the temperature at the top of the geyser and the temperature at the bottom, and with the assumption that the bubble's terminal velocity was constant and the bubble forms 15cm below the surface.

flammable.

The following paragraphs describe the safety precautions taken in detail.

4.1.1. Chemical Safety

Chemicals used in the cleaning and operation of the geyser are listed, along with the MSDS hazards of each:

1. Ethanol: Induces drowsiness, and dehydrates on chronic exposure. It is also toxic if inhaled in large quantities and is flammable.
2. conc. HNO_3 : Extremely corrosive
3. conc. HCl: Extremely corrosive
4. KOH Flakes: Corrosive.
5. Aqua Regia (from HNO_3 and HCl): Extremely corrosive, and reacts with most metals to form poisonous compounds. Also, gives off toxic NO_x gases.
6. Base Bath: (Ethanol and KOH): Basic solution, dissolves organic material.

Cleaning of the geyser is carried out in a separate well ventilated room, in an acid resistant fume hood. Adequate personal protective equipment (PPE) is required. Unsupported nitril gloves (Fischer Scientific), butyl acid resistant apron, ventilated eye protection, and working behind a sash which shields the face from the fume hood is required. Additionally, the presence of a second person is required as a safety measure. During the operation of the geyser, it is kept inside the fume hood to prevent ethanol vapours from leaking into the lab.

4.1.2. Structural Safety

The thickness of the wall of the geyser is 2.8 mm. A glass sphere of this thickness can withstand up to 4.1 bar (60 PSIA) with a safety factor of 4.

During the operation of the geyser, when a nucleation occurs, the pressure rises to the vapour pressure of the active liquid at the operating temperature (see Figure 4.1.1 for Ethanol). From Figure 4.1.1, it may be concluded that for ethanol the operating temperature should never exceed 120 °C.

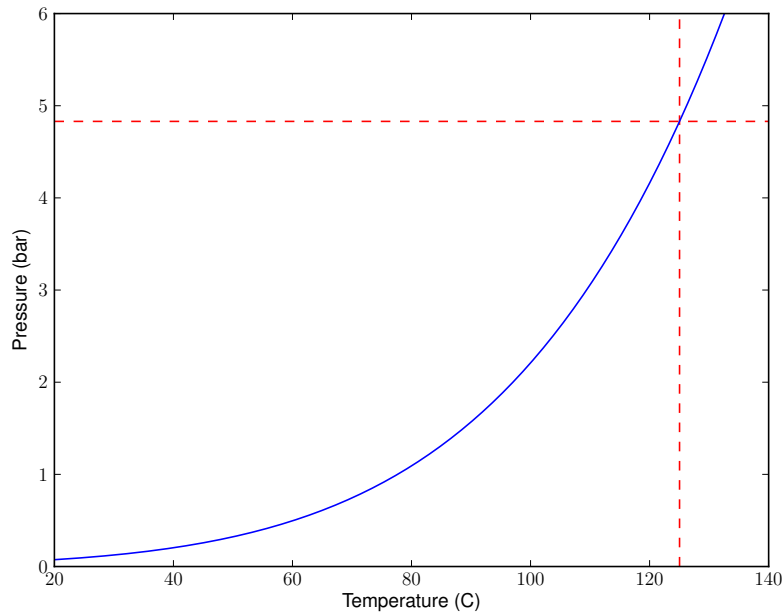


Figure 4.1.1.: Vapour pressure of ethanol predicted by the Antoine equation [32]. The red dashed line represents the limit of the geyser vessel.

Under standard operating conditions for the geyser the internal pressure is 0.138 bar (2 PSIA). When a nucleation occurs, there is a pressure spike of 2.1-4.1 bar (30-60 PSIA) depending on the operating temperature. In order to not endanger the geyser, the glass structure must be capable of handling the pressure excursions. The geometry of the geyser a sphere, permits uniform distribution of the forces acting on the glass wall when in operation. Additionally, the geyser has been tested by heating the alcohol in controlled conditions until

the internal pressure reached 4.83 bar (70 PSIA) without mechanical failure.

4.1.3. Fire Safety

The active volume fluid in the prototype, ethanol, is flammable. Hence the entire experiment is operated inside a contained volume. The geyser is kept under vacuum when running and if the vacuum fails indicating a leak, the electronic controller will immediately shut the experiment down. The micro-controller is programmed to detect changes in pressure and monitors if the pressure decreases below a set point of 0.41 bar (6 PSIA) within 30 seconds after a trigger. If it does not, the failure mode triggers and the experiment is halted with a subsequent alert to the operator. There are wires carrying line voltage to the heating system near the flammable liquid and care is taken to properly arrange the wiring to separate line voltage from signal cables. Additionally, a visual check of the wires is performed before each run to ensure the insulation is intact.

4.2. Development of the Geyser

The original geyser detector was proposed by B.Hahn and H.W. Reist in 1974 [33]. A diagram of their detector is presented in Figure 4.2.1. In this design a superheated liquid filled in the bottom chamber the top was cooled using a condenser. Nucleation caused bubbles in the superheated fluid and the vapour was condensed to liquid by the condenser. This is a modified version

4.2 Development of the Geyser

of a standard bubble chamber. The active liquid used in this early example was Methanol (boiling point: 65 °C at 1 bar) operated at 56 - 70 °C. It was successfully used to detect fission products.

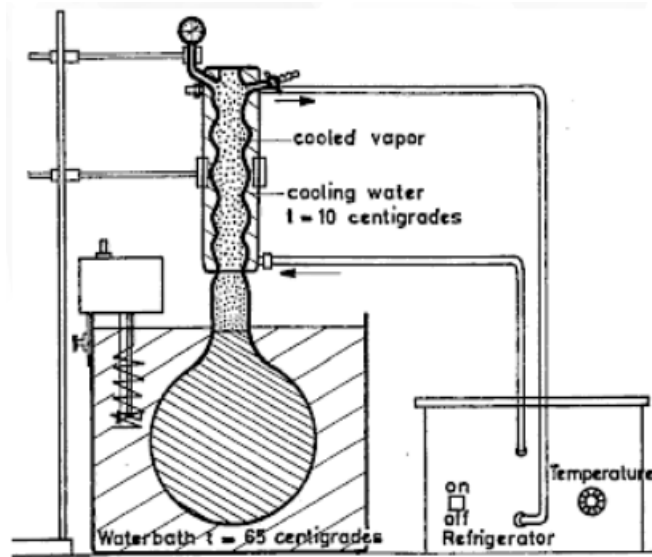


Figure 4.2.1.: The geyser detector as built by Hahn and Reist [33].

Hahn and Reist's geyser had a low degree of superheat, the difference between the temperature of the liquid when it is superheated and its boiling point, of 5-10 °C. While this is adequate to detect of fission products a version of the geyser built for PICASSO would requires much larger superheats of 70-100°C in ethanol and 50 °C in Freon-10 to detect neutrons and perform WIMP searches with a very low threshold energy.

4.2.1. The Geyser Prototype

The design of the geyser prototype was based on simplicity in construction, the experience of earlier prototypes, and the efficiency to retain the reverse

4.2 Development of the Geyser

gradient system (explained in subsection 4.2.1.1). The design of the geyser prototype is shown in Figure 4.2.2.

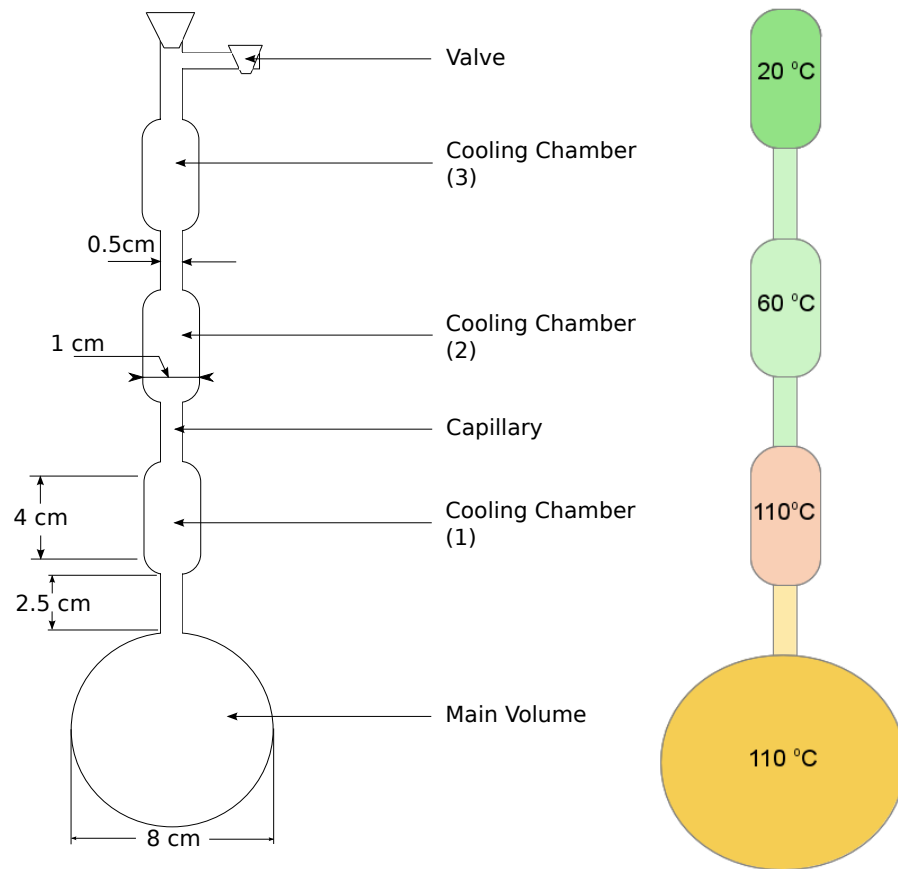


Figure 4.2.2.: Geyser - Design and reverse thermal gradient.

4.2.1.1. Geometry: The Reverse Gradient System

The geyser's fluid recovery system is based on a reverse thermal gradient. The principle is that inside the cooling chambers of the geyser a thermal gradient is established, where the bottom chamber (refer to Figure 4.2.2, cooling

chamber 1) is operated at a higher temperature (close to, or higher than, the temperature of the active liquid in the main volume), and gradually becomes colder at the top. When bubbles created at the main volume pass through a cooling chamber, they mix with the cooler liquid, and partially condense back into their liquid state. As the bubbles rise, fresh liquid replenishes the volume depleted by the bubble.

The chambers are separated from each other by capillaries of 0.5 cm inner diameter, 2.5 cm length and 1 cm outer diameter. In the geyser, convection will always be present. However, the geometry and thermal design minimizes convection in the main volume. Convection is slow in capillaries because the pressure differential and the rate of flow across a capillary depends on the radius. The rate is approximated by the Hagen-Poiseuille equation if the flow is laminar. While the flow in the geyser is not laminar, it is still slow with no observable turbulence. Hence, the rate of flow depends on the radius. Geyser 3 had three orifices of different radii (0.3 cm, 0.5 cm and 0.7 cm). From the experience of geyser 3, a radius of 0.5 cm was chosen, since rate of flow is small but the size is large enough to let bubbles break into smaller ones and pass. A full model of this phenomenon will require a computational fluid flow analysis.

With this geometry heat is supplied and extracted fast enough such that a stable gradient may be maintained. It was demonstrated that a difference of 40 °C could be achieved between two chambers. Overall, the 3 chambers provide a potential temperature difference of 120 °C between the top and the bottom, although only a difference of 100 °C was demonstrated with the available cooling system. When a nucleation occurs in the geyser, the bubble

rises while the surrounding liquid cools. The capillaries break the bubble into smaller bubbles until the gas condenses back into liquid form.

The cooling is separated from the bottom chamber by an extra chamber in the middle to minimize internal convection effects. A schematic of the temperatures at operation is shown on the right side of Figure 4.2.2.

4.2.1.2. Thermal Control

The temperature control of the main volume is provided by an oil bath which provides a uniform heating. The oil bath is heated using a hotplate, but is cooled by atmospheric heat loss. An asymmetric PID algorithm controls the temperature of the mineral oil bath. Additionally, in some cases a fan is used in the oil to improve the uniformity in temperature. Cooling is provided by peltier cell junctions which can be controlled with the help of a switching circuit. Additionally, one of the heatsinks was replaced with a custom made water cooled heatsink to increase the cooling capacity of the peltier cell. Thermocouples are attached to each chamber and are used to monitor the temperature. A temperature calibration was also performed.

4.2.1.3. Sealing of the connection between glass and metal

The connection between the glass wall of the geysler and the steel tube which connects the vacuum line is non-trivial. The top of the geysler is under vacuum, creating a lower boiling point and a higher degree of superheat. However, when a bubble forms, the connection will be subject to a pressure change from

a partial vacuum to about 2.7 bar (40 PSI). It must be able to withstand this excursion without leaking. Many types of connections were evaluated, including CAJON fittings and welded glass-metal joints. However the cleaning procedure employed uses strong acids and thus metallic joints may not be used. An o-ring seal, with a viton o-ring was used in the geysler prototype. Viton seals the glass surfaces well and the system has been shown to hold vacuum for long periods (months). The vacuum is also robust during the pressure spikes associated with normal operation.

The ability to control the bubble size inside the geysler depends on the ability to control the empty volume above the liquid. The space in the tube leading to the transducer is hard to control and in turn, it becomes difficult to control the size of the bubble. This is also directly related to the dead time of the geysler. When the bubbles are smaller, they take less time and energy to cool and hence the geysler's dead time decreases.

4.2.1.4. Controlling the liquid level and streaming

The geysler's glass walls are not smooth at a microscopic level and the vessel is therefore susceptible to streaming nucleation. A streaming nucleation is a continuous nucleation originating at one location of the container. However, this effect can be minimized by adjusting the liquid level. Figure 4.2.3 illustrates the reason behind the streaming nucleations.

When a bubble is formed, and especially if the liquid hasn't been degassed, tiny gas volumes adhere to crevices of the glass wall. This can cause

secondary nucleation, and in some cases, streaming nucleations. There are two ways to stop this process:

1. Cool the liquid below the boiling point and re-heat
2. Increase the pressure until the nucleation stops and then reduce the pressure.

Thermal control of this process induces a large dead time since to superheat a liquid it needs to be slowly heated. Hence, a pressure control is required. However in the geysier, this control can be achieved without any external pressurization. The volume above the liquid is controlled to gain control over the bubble size. If the bubble size is small enough it does not come into contact with a large fraction of the detector. This also raises the pressure naturally to the vapour pressure of the liquid, and then it drops gradually. This helps wet the surface sufficiently to drive out gas-pockets and to prevent streaming nucleations. In most cases, streaming nucleations occurs near the neck of the detector since this is where the bubble breaks into smaller parts due to the small capillary and achieves a sufficient time of contact as shown in Figure 4.2.3. When the geysier was initially designed, all three chambers were meant to be used for cooling. However, a later modification changed the bottom chamber to be heated. Thus the concept of cooling the gas until it dissolves was not realized. The bubbles do not fully get re-condensed into the liquid before they can leave the liquid. Once they leave the liquid they re-condense back to the liquid to establish the vapour pressure equilibrium on the liquid surface but slower than the ideal system.

4.3 Bubble Lifecycle

If the liquid has not been properly degassed streaming nucleations would occur even in the absence of bubble triggers. Properly degassing the detector consists of applying a vacuum while heating the active liquid to 90 °C. It requires approximately 30 minutes to 1 hour to complete the degassing cycle. Once degassed the streaming nucleations and spurious wall nucleations are eliminated.

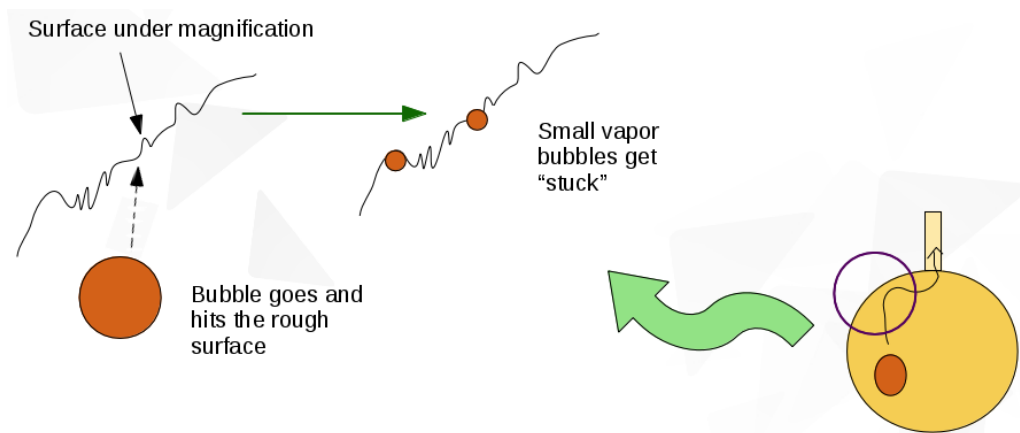


Figure 4.2.3.: Streaming and wall nucleation

4.3. Bubble Lifecycle

The lifecycle of an event begins as a small bubble in the bottom chamber as shown in Figure 4.3.1. When a bubble is formed, it takes up space, and hence, raises the pressure inside the geyser, since it is a closed system. The bubble continues to grow, until the pressure rises above the vapour pressure of the active liquid. The average diameter of the bubble is ~1 cm when it is in the bottom chamber. The bubble rises to the first chamber and at the

same time breaks into smaller pieces within the capillary. In the first chamber it does not undergo a significant reduction in size since the temperature of the first chamber is only 10-15 °C below that of the main chamber. On arrival to the 2nd chamber which is 35°C - 40 °C lower in temperature than the previous chamber, the bubble begins to be condensed rapidly. The last chamber is at 10-20 °C, where the condensation of the bubble slows down because the bubble is small at this stage and the surface area in contact with the liquid is reduced. As the bubble transits through the chambers and capillaries, the pressure reduces to the pre-nucleation value. The temperature of the active liquid also decreases since the growing nucleation bubble requires energy, which it gets from the liquid. Replenished liquid following an event experiences heat exchange from the oil bath and the remaining active liquid until thermal equilibrium is reached. The temperature cycle when a bubble forms has not been measured in the geyser prototype because it is practically not possible without disturbing the superheated state and creating instability. However temperature changes when a bubble is formed were measured by temperature probes in the small chambers. Figure 5.1.4 shows the average temperature spike from the hot and cold liquids mixing in the top chamber during bubble events. This data, along with the pressure evolution data was used to measure the dead time of the geyser. The average pressure evolution plot shown in Figure 5.1.3 is divided into two regions - a sharp rise and an exponential decay where the bubble is cooled by the condensation chambers and the geyser returns to operating conditions. The decays from the pressure curves were fit with an exponential decay function of average time constant

9.0 s.

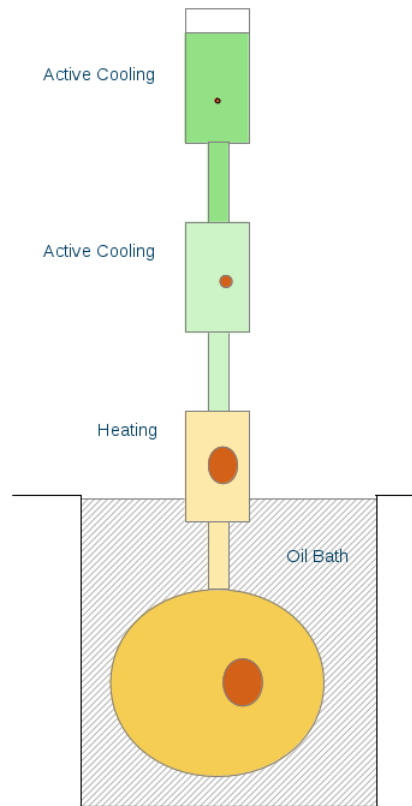


Figure 4.3.1.: Stages of bubble evolution.

4.4. Quality Control

Procedures have been developed for quality control and monitoring of the Geyser. These include cleaning, leak testing and filling/emptying procedures which are described below.

4.4.1. Cleaning

A cleaning procedure has been developed to clean the geyser of various impurities. The procedure, taking into account the cleaning of both metallic and organic impurities within the geyser is:

1. A rinse with ultrapure water (ultrapure water is defined as water with resistivity of 16 M Ω cm) at least 3 times. Water is a good solvent, and will remove a lot of impurities.
2. A rinse with salt and acetone. That is a “scrubber”. The geyser vessel is agitated during this step. The sonicator available was too small and was not effective in this process. (Duration: ~30 – ~45 min)
3. A base bath (mixture of KOH and to remove organic impurities and etch a layer of the glass itself) is used with a maximum duration should be 5 minutes.
4. Aqua-Regia (conc HCl + conc HNO₃) is then used to remove metallic impurities like Pb and Th from the glass surface.

Other reagents may be used to clean glassware but are avoided in our procedures include Chromic acid (Carcinogen), Pirhana mix (violent reaction to organic compounds / safety issue) and HF (extremely dangerous).

4.4.2. Filling and Degassing

Once a geyser is filled it is degassed by applying a vacuum. The degassing is completed in several steps. The alcohol is filled in the geyser by using a

series of filtration steps. Two funnels are used, one after another with filter paper in them. The ethanol is poured through the filtration system into the geyser. The levels of ethanol required has been measured and marked on the geyser, and it is filled to the level specified. The marking was made by taking into account the expansion of ethanol when it is heated. First, half of the bottom bulb is filled and degassed; the fluid is heated to 90 °C while under vacuum removing any trapped air. The bubbles produced during degassing mimic the expected nucleations in the geyser. When the vacuum pump is operating the possibility of liquid entering into the vacuum line is prevented by a trap system. The bottom bulb fill is completed and degassed again then; this process is repeated until the desired fluid level is reached. Each time before filling, the ethanol needs to be cooled down since ethanol forms an azeotrope with water above 31°C and it is susceptible to absorb water from the atmosphere when the geyser is opened and being filled. Cooling the ethanol reduces the amount of water absorbed. For a freon based geyser a fractional distillation method is recommended and a better system of liquid level control needs to be designed.

4.5. Electronic Control of the Geyser

The geyser is controlled by a temperature and pressure feedback loop. The hardware used for temperature measurements are J-Type thermocouples which are read out via a National Instruments NI-cFP-TC-120. The pressure readout uses an Omega PX-300AI pressure transducer and an Arduino controller board

which controls the heating.

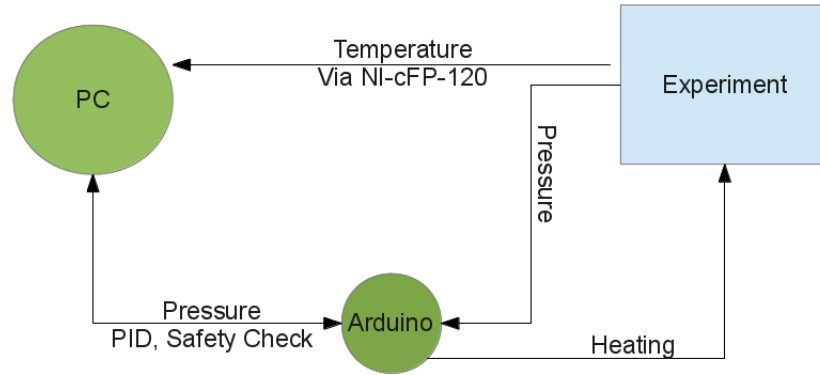


Figure 4.5.1.: Electronic control of the geyser

The Arduino is based on the ATMEL AVR 328P microcontroller which has 5 ADCs of 12 bit and 16 digital output pins from which, 6 are connected to the AVR's pulse width modulation (PWM) circuit. Analog port 0 and 1 are connected to the I2C bus on the AVR and there are 2 ports for 5V and 3.3V as well as a ground port. The pressure transducer is current based. A resistor of $416\ \Omega$ is placed between the signal and the ground cables of the transducer and the Arduino board is used to record the potential difference across the resistor and calculate the pressure. The PWM port 5 on the Arduino is connected to a solid state relay which is connected to the hot plate. A schematic is shown in Figure 4.5.2. The Arduino is programmed to relay data about the pressure at a rate of 10Hz and accept interrupts for control of the hot plate.

Figure 4.5.1 shows a flowchart diagram of the control circuit of the geyser. A piezo-electric sensor attached to the wall of the geyser is connected to a pre-amplifier and an oscilloscope. The oscilloscope is monitored by the computer

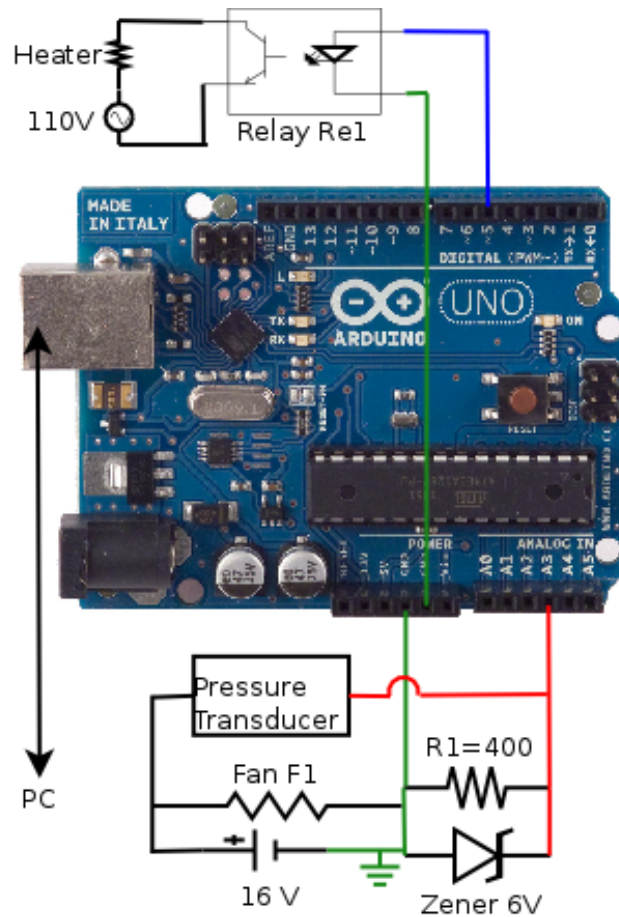


Figure 4.5.2.: The Arduino control board and circuit used for the heater controls and the pressure measurement.

using VXI (VMEbus eXtension for Instrumentation) protocol ensuring that every trigger event is stored. The piezo-electric sensor data is not used to control the experiment.

The software controlling the geyser is based on event driven programming. An incoming event, such as a pressure measurement, triggers a “dispatcher”, which then categorizes the event and sends the information to a “handler” program corresponding to the type of incoming data, and triggers

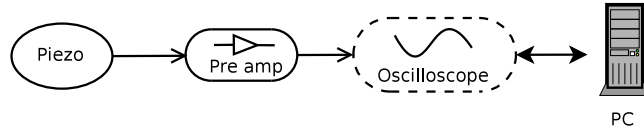


Figure 4.5.3.: Piezo-electric sensor circuit

a decision or an action that it is programmed to handle. Such programs have a “reactor loop” in their core which monitors the transport for events and launches the respective handler. For the geyser, a Python framework “Twisted” was used [34].

The program is structured into a client-server mechanism. A schematic of the program is shown in Figure 5.2.2.

1. PID Daemon: operates at 1 Hz, to calculate the relative power output needed by the heater. If a change of power is needed the daemon sends the new value to the transport.
2. PID Optimizer: runs every 10 minutes (default is OFF) to optimize the PID coefficients by the Cohen-Coon PID tuning method [35].
3. Safety Daemon: monitors the pressure and temperature. If a pressure change is observed and the pressure is not restored after a bubble event, it shuts down the experiment. A shutdown is also triggered if the temperature increases 20 °C above the set point.
4. Hardware Server: monitors the hardware and sends/receives data asynchronously to avoid packet collisions.
5. State Machine: monitors the states of the experiment, including “heating”, “stable”, “cooling” or “unstable”, controls the PID daemon, the

control interrupts, and holds target variables for geyser operation such as set temperature.

6. Control Interrupt: monitors the control interface for changes and makes the appropriate changes in the state machine's variables.

The code is available at GitHub [36]. The next chapter discusses the data, quality control of the data and the accuracy of the measuring devices.

5. Operation and Data Sources

5.1. Overview

In this chapter, the data acquisition sources and the operation of the geyser is described. Figure 5.1.1 is an illustration of the hardware used in the experiment and to record data.

5.1.1. Acoustic Data Acquisition

Piezo-electric sensor type B (larger crystal, lower gain) number PZB-0037 is used for acoustic measurements and is attached to the glass wall of the geyser by a two-component epoxy. A 20 kHz high pass filter with a rolloff of 3dB/decade is attached to the input signal before the pre-amp. The pre-amp is an inverting amplifier with a high impedance JFET op-amp, TL-071 with a unity gain bandwidth of 3 Mhz (see Figure 4.5.3). The pre-amp is connected to an oscilloscope (Tektronix DPO 5000), with a sampling frequency of 1.25 Mhz and 50,000 samples per time window. The data is collected by a PC using the VMEBus eXtension for Instrumentation protocol over ethernet. This uses

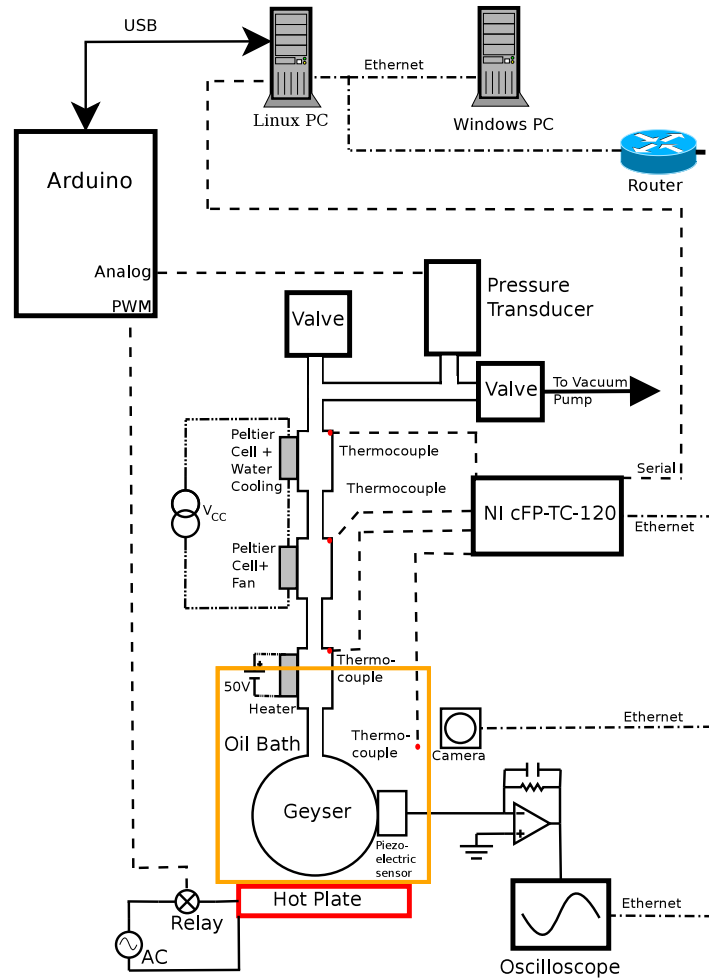


Figure 5.1.1.: Data acquisition and control system of the geyser

GPIB commands over Remote Procedure Call (RPC), which is an open source protocol. Collection of the data is handled by an asynchronous state machine. A process “dispatcher” monitors for any triggers from the oscilloscope over the TCP/VXI interface. Once a trigger is detected the dispatcher launches a new thread “handler” to obtain the data from the oscilloscope and store it while the dispatcher is immediately freed to monitor the next trigger signal. This significantly reduces the dead time, since the process is not blocked while data

transfer and storage takes place.

Each event is stored as a binary file where every 2 bytes denote an ADC value. The events each have 50,000 samples each resulting in a 100kB binary file storing the raw data. Each trigger is accompanied by a text file which stores information about the trigger itself. The wfi files contain information related to the scope settings. The contents of a wfi file has been described in Appendix A. Additional GPIB over TCP/VXI commands are available as described in the Tektronix manual for GPIB control of scopes. They can be added as necessary.

In the geyser experiment, the entire information about an event lies within the first scope trace generated by the event. The acoustic signal of a typical event is shown in Figure 5.1.2.

The acoustic system may trigger on noise not associated with a bubble that may originate from electronic noise or actual piezo-electric sensor signals from vibrations. The relevant types of noise observed from the piezo-electric sensor can be classified as follows:

1. Piezo-electric sensor triggers to external vibrations: construction in the building, closing doors and any vibration by a heavy object dropping in the lab can cause this kind of noise.
2. Bubbles in the oil bath: if the mineral oil used in heating becomes contaminated with water, bubbles are produced. They have the same profile as a nucleation bubble in the geyser.
3. Noise from vibrations within the system: the stirring fan, water cooling

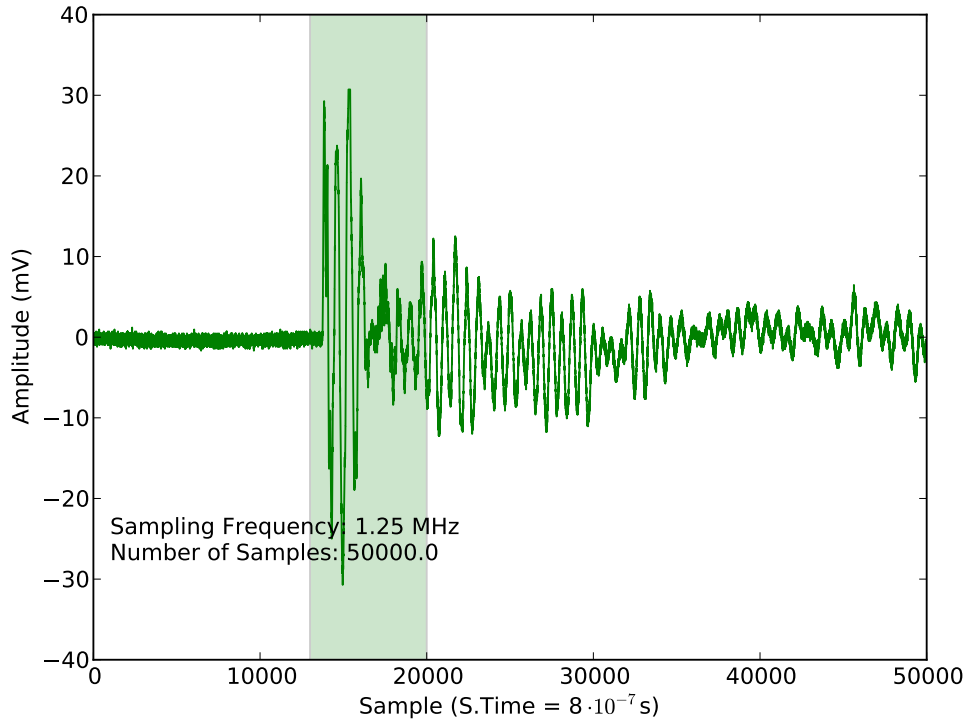


Figure 5.1.2.: Acoustic data of an event from the geyser. The shaded area represents samples 13,000 - 20,000 region of the signal used for analysis.

and the fan cooling the upper peltier cells also add to the noise floor of the system.

There is no reliable way to clean the data from the electronic noise with the help of the piezo-electric sensor alone. The events recorded by the piezo-electric sensor were correlated to the events captured by the pressure transducer. An event needs to be recorded by the piezo-electric sensor, pressure sensor and the camera to be counted as a valid event, and used for analysis. This is described in the next section.

5.1.2. Pressure

The time resolution of the sensor is 1 ms and the pressure range is 0-6.89 bar with an accuracy of 0.25% full scale. The pressure sensor is attached to a 0.25 inch NPT steel pipe which in turn is sealed to the geyser using a viton o-ring. The o-ring seal was tested by evacuating the geyser. It was tested a second time in the operation phase of the geyser by keeping some amount of air, and letting the expansion of the liquid compress it to 4.8 bar. The seal holds vacuum of 0.0013 bar which is comparable to the uncertainty in the measurement by the pressure transducer. The gauge is connected to a resistor of 416 Ω , and a 6 V Zener diode. The Zener diode (see Figure 4.5.2) prevents an overvoltage which could damage the microcontroller. The voltage across the resistor is recorded by the microcontroller ADC at 10Hz with a resolution of 5V/1024 units or 0.0049 V per unit. The ADC clock is 16 MHz divided by a pre-scale factor of 128 (16MHz/128 = 125 KHz). A conversion requires 13 ADC clocks and the sample rate is therefore about 125KHz/13 or 9600 Hz. COUPP (another dark matter search experiment using bubble chambers) uses fast pressure measurements during the formation of the bubble at 1 kHz for discrimination between wall events and bulk events. Hence, a future improvement which could be made is the acquisition of 1 kHz pressure data.

The data is transmitted to a PC using a serial interface. Again, an asynchronous server was used for handling the pressure data. Since the pressure and PID control are handled by the same serial line, the server controlling

the hardware is designed to handle collisions by using queues. A dispatcher handles the inbound/outbound requests to and from the hardware, and the dispatcher gets/sends the data and then hands the data over to a handler routine, which then sorts the data converts ADC units to pressure values and pushes it to the server's memory making it available to other routines. Figure 5.1.3 shows a pressure evolution curve of a bubble event. A pressure cycle can be divided into 2 regions - a sharp rise, and a decay. The decay of the pressure spike has been fit with an exponential decay function. The time constant is 9.9 s. In addition to the exponential decay, an oscillation of the pressure is observed. The oscillation does not appear to be harmonic and has not been studied further. One possible reason for these variations is the fact that small bubbles have to "squeeze" through the capillaries and chambers before they move to the surface.

5.1.3. Temperature

The temperature is recorded by 4 J-Type thermocouples in the mineral oil, and each of the chambers respectively. The thermocouples are connected to a National Instruments NI-cFP-TC-120 compact fieldpoint module with a time resolution of 1.2 seconds. The module is connected to a PC via a serial port and by ethernet. The serial port is used by the same hardware daemon controlling the micro-controller. The temperature of the mineral oil is transmitted using the OptoMux protocol, an ASCII based challenge-response protocol used for controlling devices on a serial bus. This is done so that the entire controller daemon gets a unified interface for all its inputs and outputs. Another com-

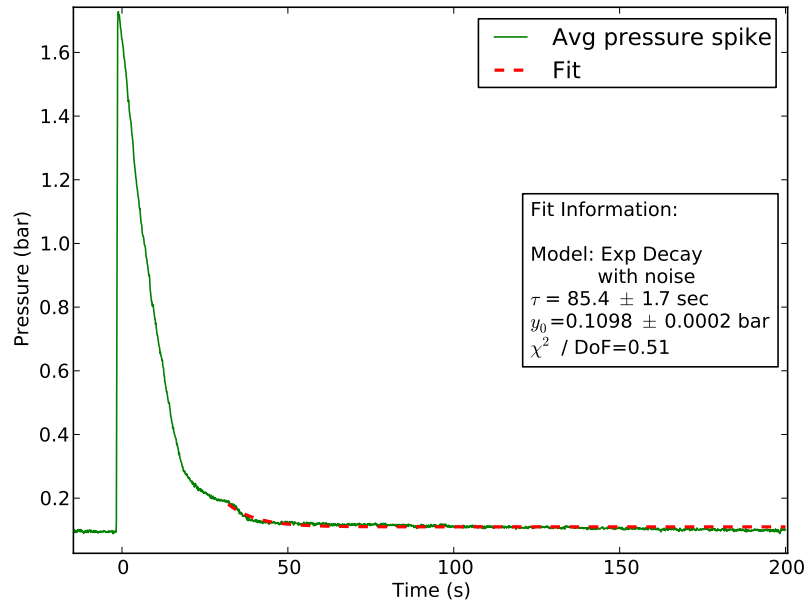


Figure 5.1.3.: Average pressure changes in a bubble evolution. The dead time is driven by the trailing edge, and has been fitted with an exponential decay with flat background.

puter records the temperatures using LabView over the ethernet interface and stores them. This data is not used by the control algorithm, and may be processed offline. An additional SMBus (Simple Management bus, two-wire lightweight communication system) infrared thermometer is attached to the micro-controller and can be used to measure the temperature of the geyser at any point where it is too difficult to attach a thermocouple (usually glass walls).

During each event the thermocouples register a detectable temperature excursion, due to the hot and cold liquids mixing. Based on the chamber for which a measurement is taken, it can be an excursion where the liquid becomes

cooler (bottom chamber), or the reverse (the top chamber). This gives us an additional measure of the dead time. The average of all such spikes from alpha runs is shown in Figure 5.1.4. The time constants of the temperature excursions in the two chambers are consistent. To accurately determine the dead time, a measurement of the temperature of the active liquid would be required. Comparing Figure 5.1.3 and Figure 5.1.4, it is obvious that the dead time of the system is determined by the temperatures. Based on event rates, the dead time is of the order of the decay time τ .

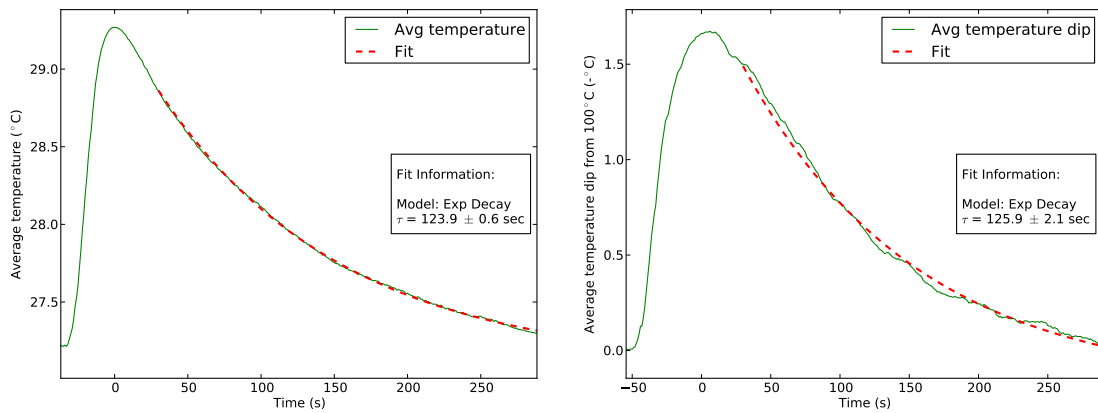


Figure 5.1.4.: (Left) Average temperature excursion in the top chamber measured during alpha runs. (Right) Average temperature dip in the bottom chamber measured during alpha runs.

5.1.4. Optical Data Taking

Pictures of events are acquired by an Axis M3011HD camera with a resolution of 1 megapixel and frame rate of 30fps. The camera has an internal motion sensor which is set to detect bubbles in the active volume of the geyser. The

camera is set to take 20 frames in 1 second before each trigger. Due to a memory corruption issue that limit the camera to 20fps instead of the 30fps specification. This is sufficient to locate the position of a bubble inside the detector. The event images associated with it and are automatically uploaded to the PC via an FTP service, are time stamped so that they can be correlates with the piezo-electric sensor signals. Figure 5.1.5 shows a mask of the region used with the motion detection algorithm to trigger on events.

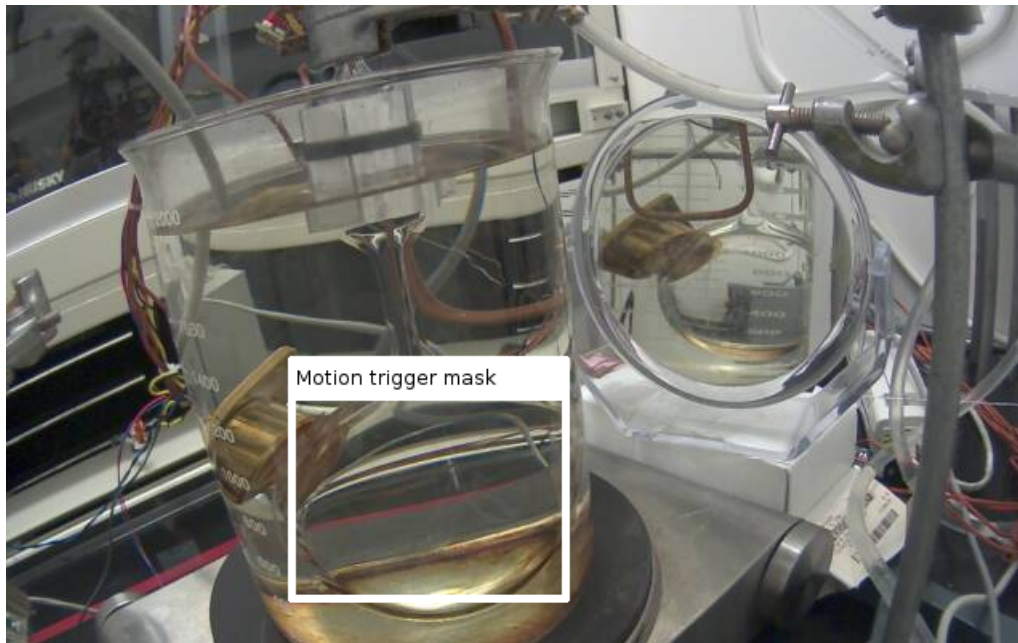


Figure 5.1.5.: Camera image of the experiment. The region selected for the motion triggers is indicated by the rectangle.

5.2. Data flow

Figure 5.2.1 provides an illustration of the data flow organization, divided into 3 parts, the hardware server, control algorithm and data recorder.

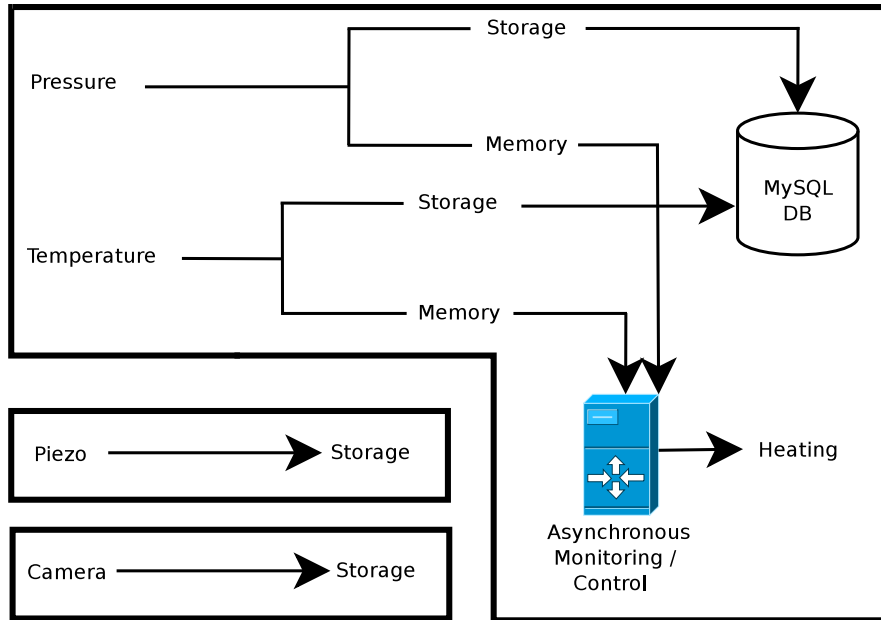


Figure 5.2.1.: Schematics of data flow of the geyser.

5.2.1. Hardware Server

The hardware server is a program that performs tasks according to the schematics shown in Figure 5.2.2. The hardware server is implemented using the “Twisted” framework for python [34]. It is asynchronous and event driven. The code interfaces the hardware and provides a web server interface to other modules. The server handles the I/O scheduling and avoids packet collisions on all buses. The core of the code is called the reactor pattern which is essentially a service which handles requests from multiple inputs using the `epoll7` implementation [34]. It demultiplexes the requests and synchronously delivers them to handlers. From here, the handlers detach themselves into separate threads. This system was chosen because of its stability over conventional code. An error in execution is identified by using `ErrBacks` (callbacks issued

in case an error is raised), and handled before it reaches the core. Even if the error does reach the core, it is logged and the server continues operating. This is required for reliability since the geyser may explode if it reaches an uncontrolled state. This daemon process runs at start up, and should never be turned off. In addition to this process, checks have been designed and coded into the microcontroller to prevent the geyser from reaching dangerous conditions at all times. This is an added safety system which does not rely on the computer, and thus is more reliable and suited for this condition.

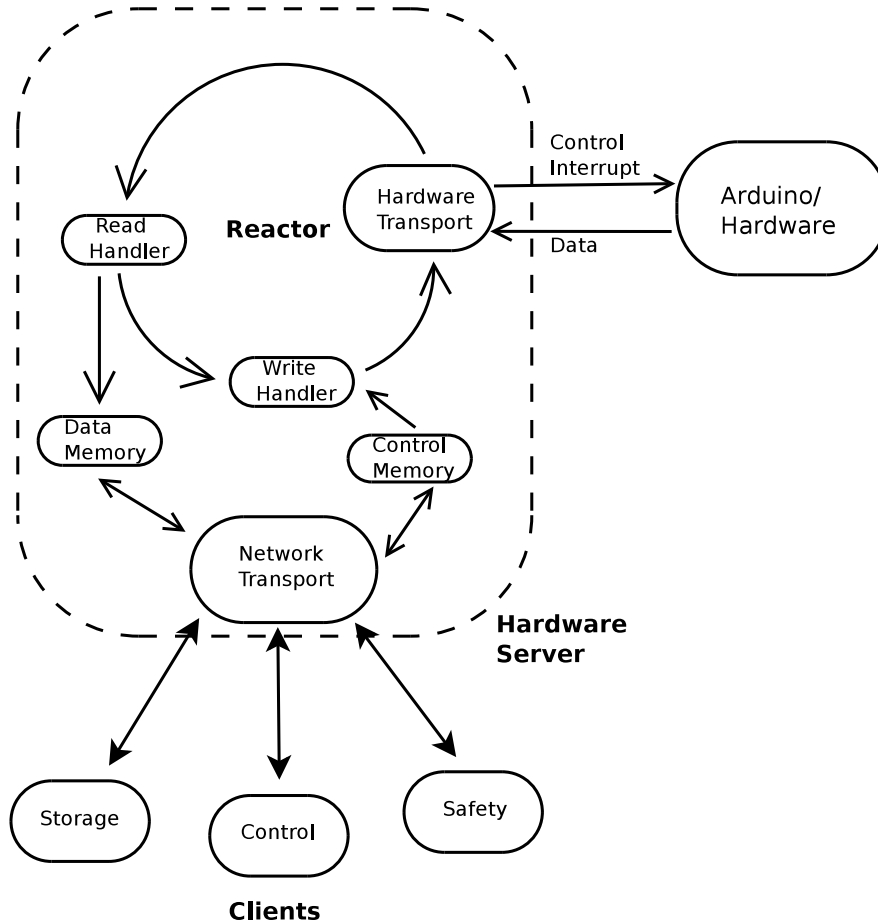


Figure 5.2.2.: A schematic of the hardware interfacing program.

5.2.2. Geyser Control Algorithms

The control and monitoring interface is web based and can be accessed remotely. The interface connects with the hardware server over the network and permits control of the experiment. Each time a run is started, the system automatically assigns a new run number. The temperature and pressure data are recorded in a MySQL database hosted on the same machine that cannot be modified. The database can be cloned at anytime to any other machine for analysis work. The history of each run and the run parameters such as temperature, set temperature and pressure are stored in the system.

5.2.2.1. Acoustic Data Recording

An independent program is used exclusively to record data from the piezoelectric sensor. This is separated from the rest of the experiment since it produces substantial amounts of data and has its own data structure. The daemon controlling this data collection is similar to the one used for pressure and temperature and is based on the same framework.

5.3. Operation

5.3.1. Start of Operation

The procedure to start the geyser is as follows:

1. A check of the liquid level is done to ensure that the geyser is evacuated.

This can be established by checking the pressure is between 0.69-0.14 bar. This is the normal range for the vapour pressure of ethanol at room temperature.

2. The cooling water for the peltier cells is started. This system is prone to leakage if the pressure is too high. After confirming that there are no leaks the power supply to the peltier cells is switched on.
3. The power supply for the heating element on the bottom chamber is switched on.
4. If the hardware server is not running, start it. Then start the State Machine daemon.
5. Commence a run using the web interface.
6. Commence the acoustic data recorder.

5.3.2. End of Operation

To stop the geyser the procedure is:

1. Set the operating temperature to 0 which stops the heating system.
2. Click “Change Geyser Status: OFF” on the web interface. This will cycle the run number.
3. Turn off the acoustic data recorder. (Ctrl-C)
4. Turn off the peliter. If not done, ice forms around the peltier over time. This should be avoided.
5. Turn off the heating element and close the peltier cell cooling lines.

5.4. Data quality:

5.4.1. Correlation of Data Sources

The data from all the sensors are received and stored in binary databases with time stamps as the primary index. However, any one signal cannot be relied upon to reconstruct an event. This system also serves to check the trigger level of the piezo-electric sensor by confirming a trigger to every event identified by the images and the pressure sensor. An event is labeled as good if it has all 3 sources of data (pressure, picture, acoustics) are associated. The event is then stored in a database called “EventPassport” and is available for analysis.

5.4.2. Stability of the Superheat

A study of the stability of the geyser over time was performed to check the data quality and filter bad runs from the analysis. For this study the pressure, temperature and superheat stability of the geyser during different runs was checked, and a comparison was made between superheats and the average PVar (Explained in section 6.2). Figure 5.4.1 and Figure 5.4.2 show the pressure and temperature in the runs considered for analysis respectively. Runs 195 and 196 have a lower pressure because the vacuum pump was used to degas the geyser prior to running. In run 201, a peltier cell was nonfunctional due to a water leakage. This explains the elevated pressure during this run. Table A.1 shows a summary of the runs considered for analysis.

Electronic noise levels were also compared from run to run to test the

stability of the acoustic system.

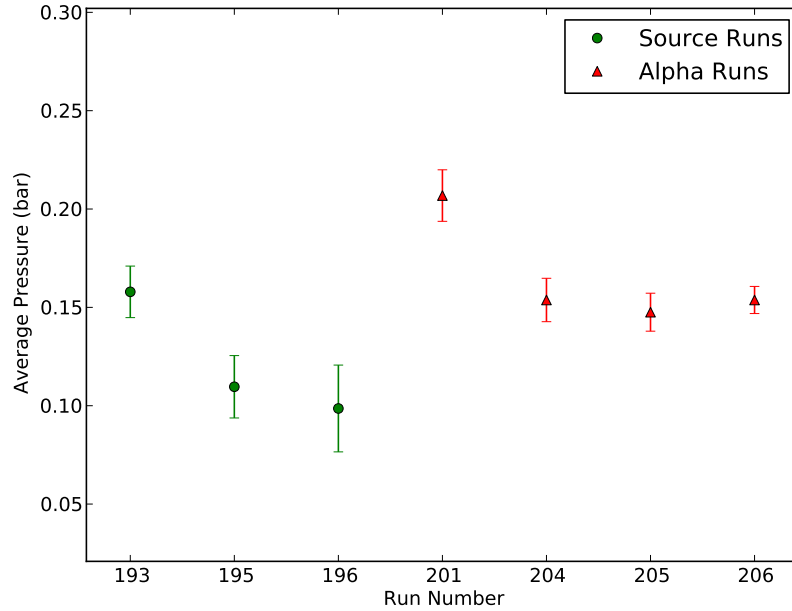


Figure 5.4.1.: Average pressures runs considered for analysis.

Figure 5.4.3 shows the superheat in each run based on the temperature and the pressure data presented in Figure 5.4.1 and Figure 5.4.2. A comparison of PVar was performed for the calibration runs 193, 195 and 196 to study the scale of the effect of the change of superheat. The change is minimal, and is discussed in the section discussing PVar in Chapter 6.

5.5. Limitations of the Geyser.

The geyser has a few limitations and the operator has to be careful to not stress the geyser and its safety mechanisms. The geyser vessel has been designed for

5.5 Limitations of the Geyser.

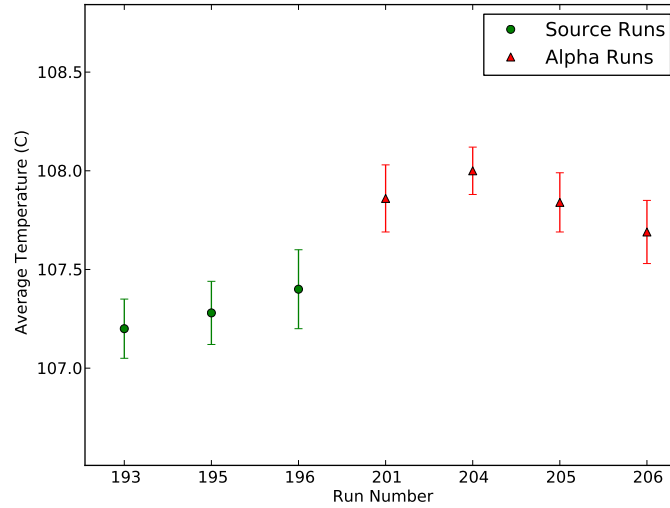


Figure 5.4.2.: Average temperatures in runs considered for analysis. Note: The temperature was measured in the oil bath.

4.13 bar with a safety factor 4 meaning, using ethanol as the fiducial fluid, the operating temperature should not exceed 120° C. The vessel has also been tested at 4.83 bar and is safe for operation at its design limits. Excess pressure may cause cracks to develop in the geyser. When the geyser is heated, the liquid expands and occupies more volume than at room temperature. Care must be taken to not overfill the geyser since once it expands to fill the entire volume, the pressure will rise above 4.83 bar. Increasing this pressure, the o-ring in the glass to metal joint may begin to leak or the geyser would fracture. In the event the geyser is subjected to pressures exceeding 4.83 bar, the o-ring must be checked before resuming operation. A log book is maintained where every run is recorded and incidents like overpressure, cleaning, change of pre-amplifiers or other circuitry, are recorded. The current filling procedure,

5.5 Limitations of the Geyser.

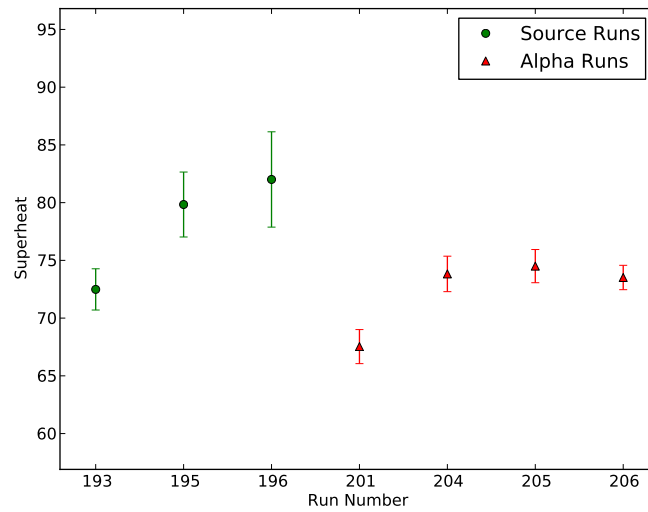


Figure 5.4.3.: Average superheat achieved in the runs

described in chapter 4, is not ideal and can introduce impurities in the geyser.

A distillation process is recommended for future geysers.

6. Analysis and Physics of the Geyser

The design and control of the geyser, data acquisition and operation has been described in subsection 4.2.1, section 5.1 and section 5.3 respectively. In this chapter, the analysis of the data is discussed.

6.1. Event Localization

The bubble identification and localization algorithm uses a quantity called “Image Entropy” to distinguish parts of an image that contain a bubble. Image Entropy provides the amount of information which an image compression algorithm will produce after processing an image. The idea is that, if there is a “bland” image (monochrome), then the compressed image will be small, but if the image contains information, which causes a change in color or hue then the size would increase. To calculate the image entropy an image is histogrammed

in the tonal distribution. The entropy then is defined as:

$$H = -\sum_i P_i \log P_i \quad (6.1.1)$$

where P_i is the bin content of the i^{th} bin in the tonal histogram divided by the total number of entries [37]. This algorithm was used iteratively to identify the locations of the bubbles.

For every event, there are 20 associated frames since 1 second of pre-buffered data is stored at 20 FPS. To analyze an event of 20 frames every frame (except frame 1) is first subtracted from the previous one, providing an image like the one illustrated in Figure 6.1.1.

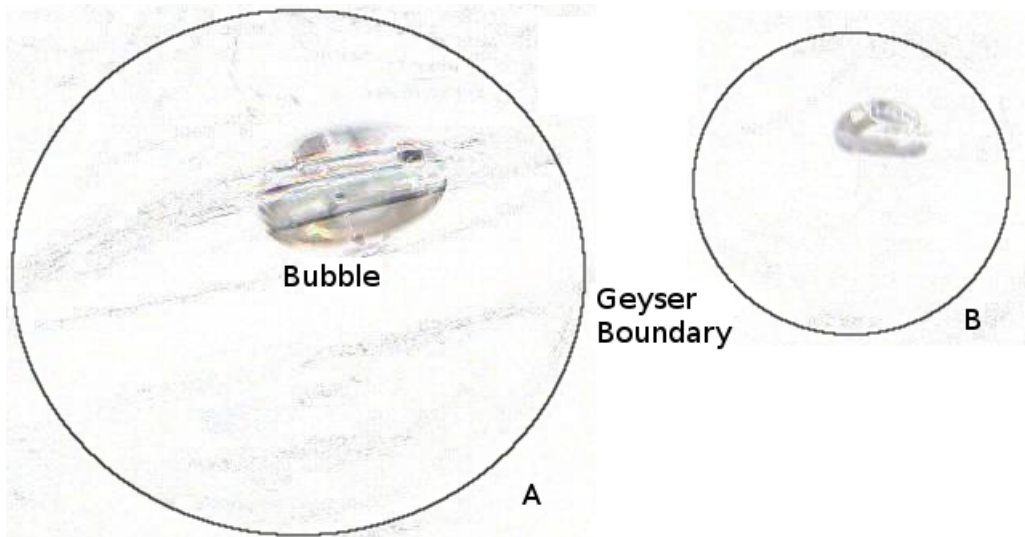


Figure 6.1.1.: The difference of frames when a nucleation occurs in (A) the main volume and (B) the mirror.

The algorithm concentrates on 2 regions of the image - the direct image

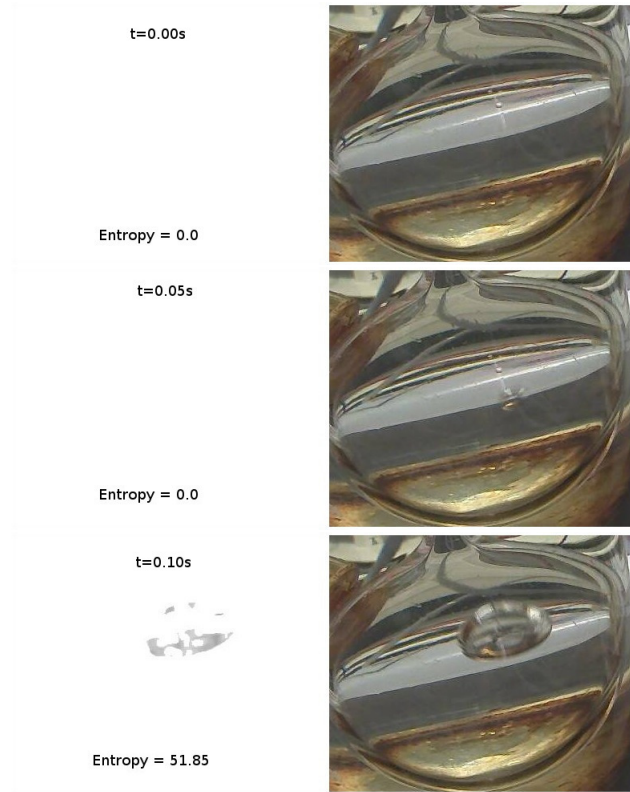


Figure 6.1.2.: Illustration showing the frame before and the frame in which the bubble is identified. On the left, is the result after the subtraction from the previous frame and the smoothing filters, on the right is the actual frame. Note: After applying smoothing filters, there is no residual on the left when the bubble is not detectable ($t=0.0s$ and $0.05s$). At $t=0.10s$ the bubble is large enough such that a residual is left after applying the smoothing filters.

of the detector and the mirror. When there are no detectable bubbles in the image, the entropy is negligible. However, when a bubble is present the entropy becomes large. Additionally the camera transmits pre-trigger images so that the bubble always appears in the 15th to 20th frame of the trigger. The algorithm uses the first 10 frames to calculate the average entropy generated by the random disturbances (as seen in Figure 6.1.1) across the image, and then establishes a threshold of $\mu + 2\sigma$ where μ is the average and σ is the

6.1 Event Localization

standard deviation, as the criteria for selecting the frame containing a bubble. Figure 6.1.1 is a picture of the difference between the frame in which the bubble has been identified and the frame just before that. Figure 6.1.2 shows an image of the frame just before the identification of the bubble and the frame where it is identified. The images on the right show the actual frame and the images on the left show the difference of frames after the smoothing filters are applied.

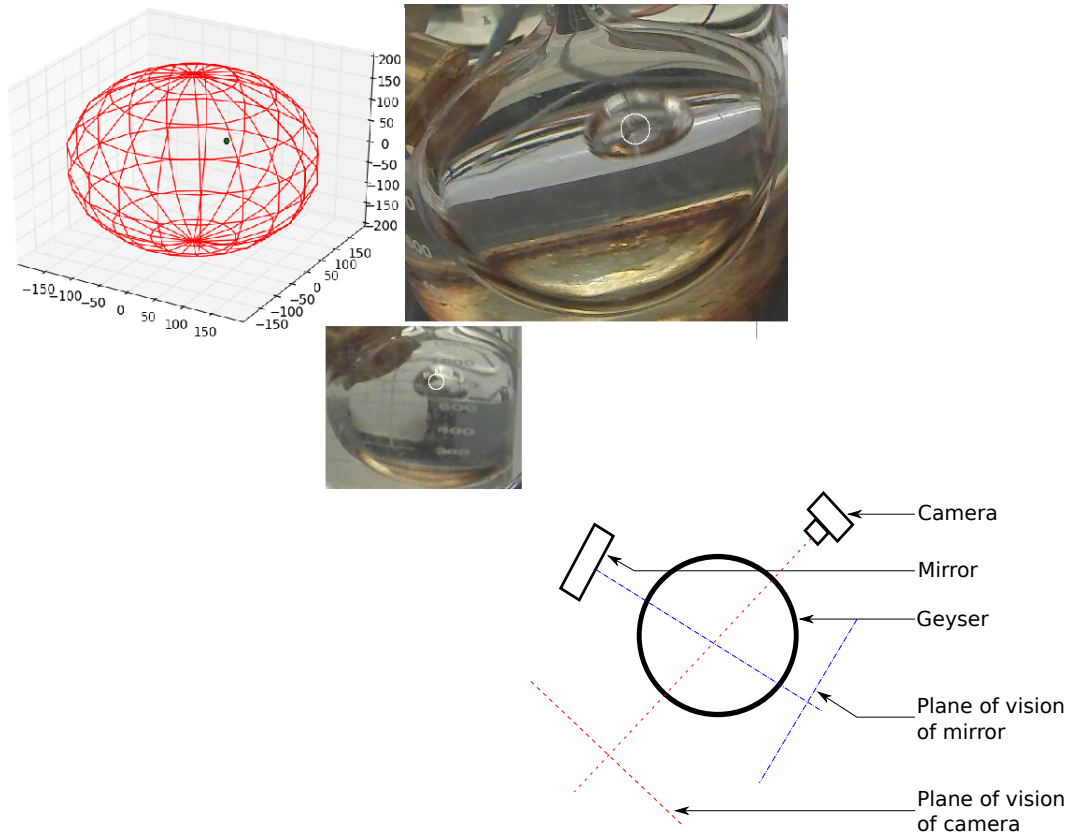


Figure 6.1.3.: (Top) An event, after processing the image. Shown here clockwise from left: 3D localization, main volume and mirror. The white circle represents the center of the bubble as identified by the image analysis algorithm. (Bottom) A schematic of the imaging set up.

Due to the size difference between the main volume and its image in a mirror, a bubble may not always be visible at the same time in both the frames. Hence, they are evaluated separately allowing the smaller minor image bubble to be identified in a later frame. After the frames are identified, a median filter and a rank filter are applied to the image to smooth the noise (sharp lines and spikes). Once the lines are smoothed the image entropy algorithm is rerun in small 5x5 pixel boxes throughout the region of interest. Each box is assigned an entropy value that indicates how much information is present. The bubble edges usually provide the maximum entropy values while parts of the image that do not contain a bubble obtain an entropy of 0. A weighted “center of gravity” of the region where the entropy is different from zero gives an estimate for the centre of the bubble and a weighted distance from the centre provides an estimate of the bubble radius. After the location of the bubble is identified in both frames the data is combined to create a 3D position of the bubble location. Since the mirror’s plane of vision (see Figure 6.1.3 bottom) is not perfectly orthogonal to the camera’s plane of vision, an angular correction is applied to the image. Additionally, a horizontal tilt of 10° is also accounted for. Due to the nature of the refraction in the detector and the mineral oil, the horizontal, vertical and the depth axes are not all equal and linear corrections are applied to scale. Nonlinear corrections due to the refraction was not applied. Figure 6.1.3 shows an illustration of an event after processing the image. A 3D plot of the event positions is presented in Figure 6.1.4 and a histogram of the bubble radii is presented in Figure 6.1.5.

A portion of the vessel is not visible on the mirror due to total internal

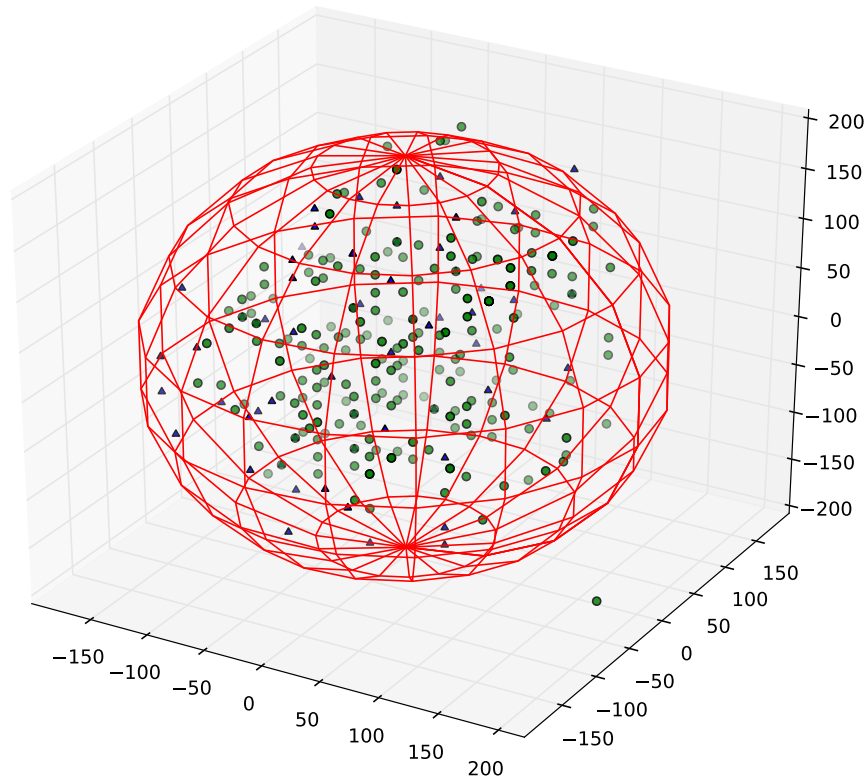


Figure 6.1.4.: 3D plot of both alpha and neutron event positions in the geysir. The green circles are neutron events and the blue triangles are alpha events.

reflection and some bubbles could not be localized along the y-axis (depth) and these were discarded. A histogram showing the distribution of the events in the geysir is shown in Figure 6.1.6. The red line is a monte-carlo of events in the geysir. The monte-carlo was performed by randomly placing events inside a sphere. The portion of the field of view blocked by total internal reflection is modeled in the monte-carlo by rejecting events from the part of the sphere which cannot be seen in the geysir prototype. The camera system is slow relative to the bubble growth. Bubbles which are near the walls cannot

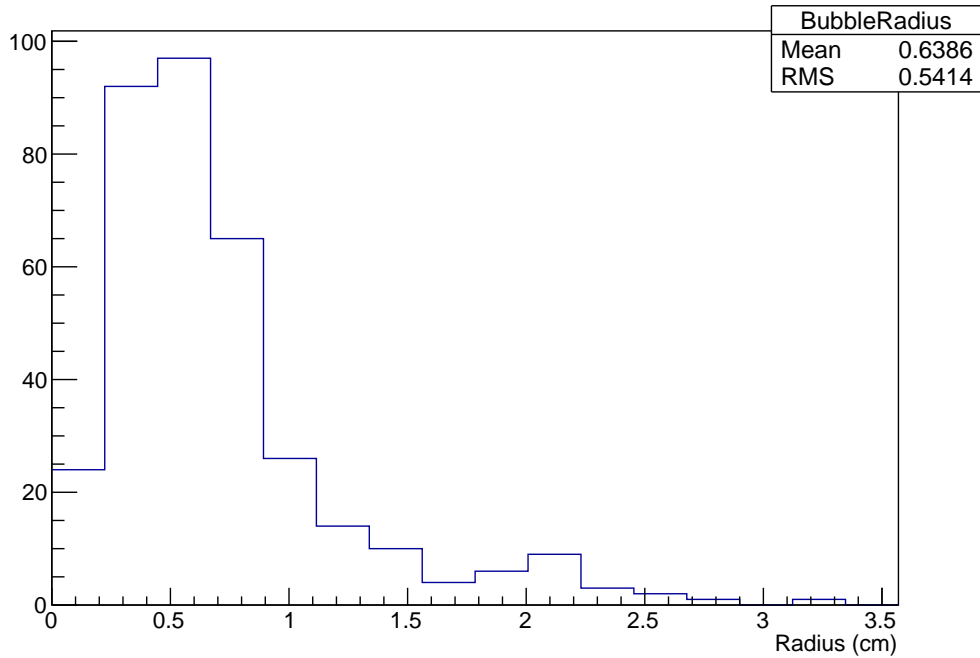


Figure 6.1.5.: Histogram of bubble radii.

expand in the direction of the wall and they have to move away from it. When the camera triggers the bubbles have already moved from their initial position and a bias is introduced in their localization. This bias was accounted for by subtracting the average bubble radius from the monte-carlo event positions close to the wall. The χ^2 between the model (monte-carlo) and the data is 3.0.

Figure 6.1.7 shows the spatial distribution of events in the geyser. In this plot, the geyser was divided into 8 equal parts by volume including the fiducial volume correction. The events were then localized inside these volumes and a histogram of the events was generated. The plot shows that the events are uniformly distributed in the detector.

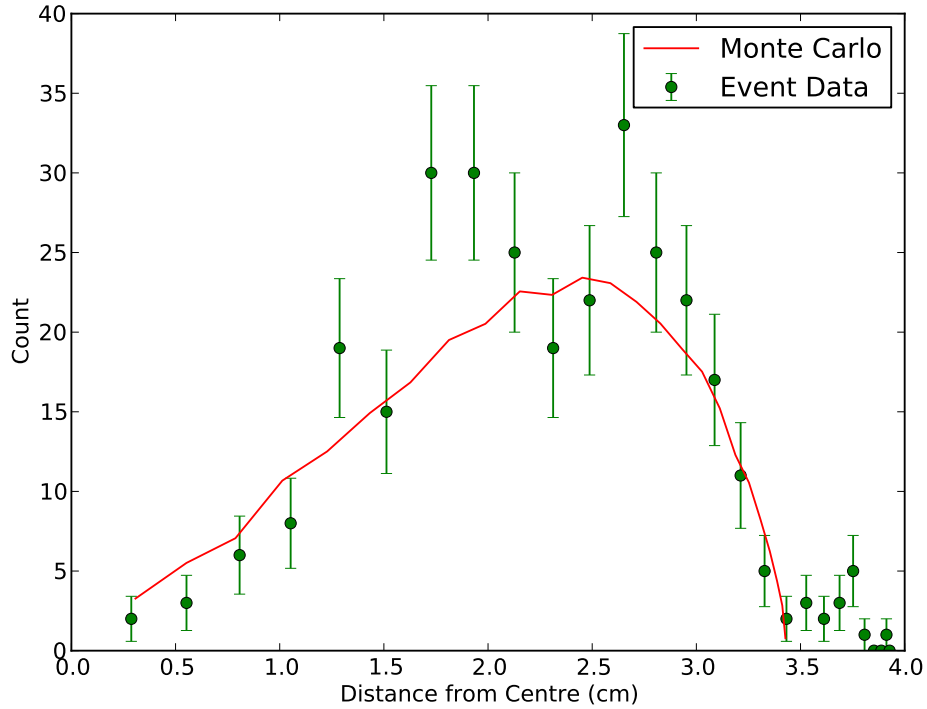


Figure 6.1.6.: 3D map of neutron events (green points) localized inside the geyser and Monte-Carlo (red line) as described in the text. The Monte-Carlo was scaled to resemble the data.

6.2. PVar

The PVar of a signal is a measurement of the deviation from an expected acoustic energy profile of a square wave. It is a variable used by the PICASSO collaboration where the algorithm to calculate PVar is:

1. Apply a frequency filter to the waveform. (20 kHz high pass in case of the geyser while typical values of 18 kHz high-pass in case of PICASSO detectors.)

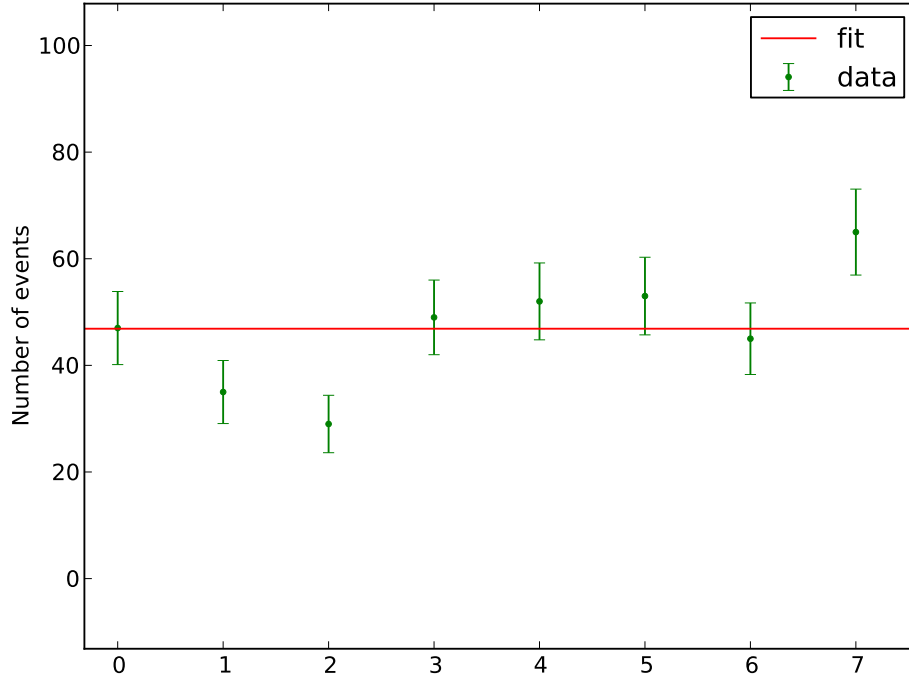


Figure 6.1.7.: Rates in equi-volume parts of the geyser. The average number of events is 47.

2. Find the power of the signal by taking the square of the amplitude.
3. Take the cumulative sum of the signal and subtract a baseline defined by a line joining 0 and the maximum of the cumulative sum.
4. Take the integral of the difference and then the log of the result.

The PICASSO Collaboration has shown [23] that a discrimination between alpha particle and recoil nucleus like events exists in PVar. For the analysis of the geyser, PVar was applied to try to observe this discrimination. Before a PVar comparison of events is done, it is necessary to compare the PVar between the neutron calibration runs to see if a difference in the superheat

makes PVar significantly different between runs thus implying a superheat correction is needed. A plot of superheat vs mean PVar in runs 193, 195, 196, 208 and 214 is shown in Figure 6.2.1. No superheat correction was deemed necessary for runs 193, 195 and 196 which were used in the following PVar discrimination analysis.

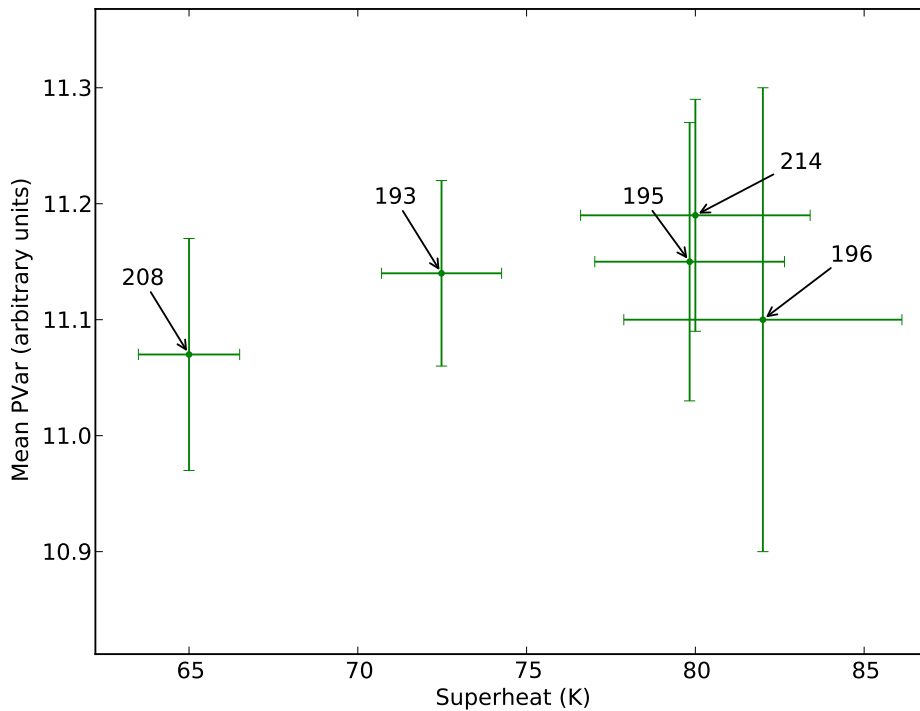


Figure 6.2.1.: Superheat vs PVar of neutron runs 193 (6h15m), 195 (4h), 196 (3h13m) and runs with new source position 208 (3h 16m) and 214 (1h 15m)

A histogram of PVar was produced for all bulk events (events that lie in within a radial distance of 3 cm from the centre of the geyser) in an alpha run are compared to all bulk events in a neutron calibration run. Events near the wall have a different acoustic signature compared to events near the center

due to the speed of sound being different in the wall and the liquid. A direct comparison of such events with the events in the bulk of the geyser is not possible and in the analysis only bulk events are considered. The source of the alpha particles in the bulk of the detector is primarily radon. Such an alpha decay creates two bubbles, one from the Bragg peak and the other from nuclear recoil. This is the reason behind the acoustic energy being larger in radon induced events compared to neutron induced events. It can be concluded that a discrimination exists between alpha and neutron events in the geyser. An 81.3% separation between the alpha and the neutrons were found by taking $1 - \frac{C}{A}$ where C is the common area under both histograms and A is the area of the histogram of alpha particles (red).

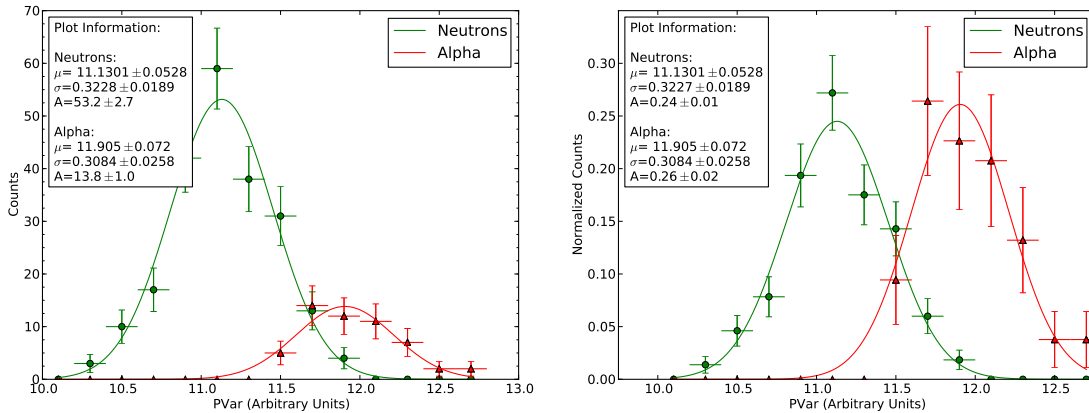


Figure 6.2.2.: (Left) Pvar histogram of alpha and source runs. (Right) Normalized PVar histograms used for calculation of discrimination.

6.3. gFVar

The average Discrete Fourier Transform (DFT) spectrum of the events in the source runs 193,195 and 196 vs events in alpha runs 201, 204, 205 and 206 runs were revisited to check if a variable can be constructed which gives a better discrimination. A plot of the average scaled DFTs (Amplitude $\times \omega^2$ vs frequency f , where $\omega = 2\pi f$) from source and alpha runs is shown in Figure 6.3.1.

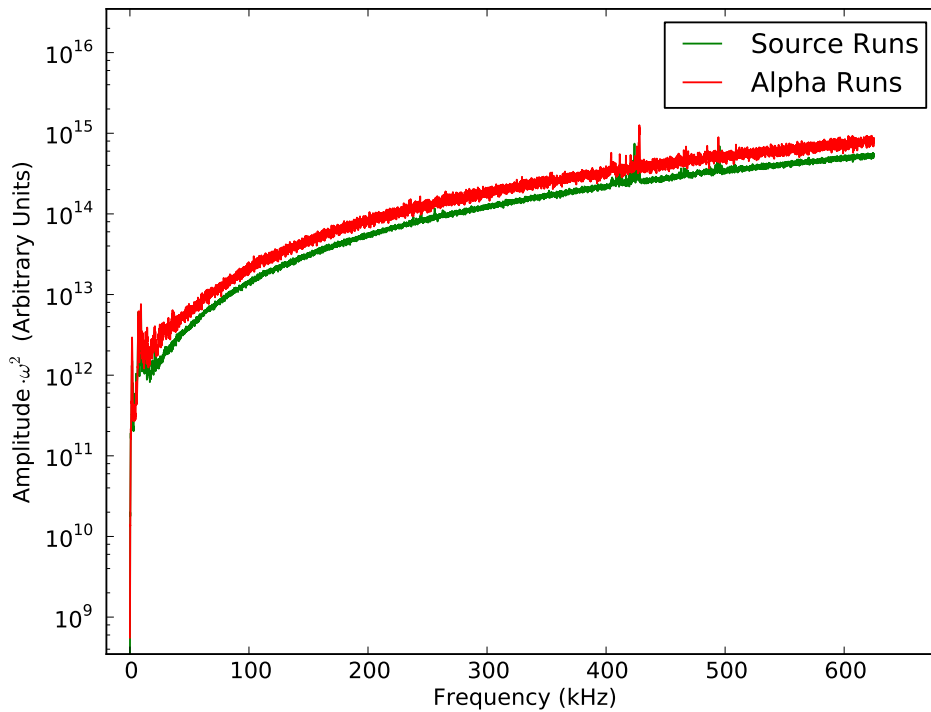


Figure 6.3.1.: Average of scaled DFTs from source run events and alpha run events.

Just like with PVar, before gFVar comparison of events is completed, it is

6.3 gFVar

necessary to compare the gFVar between the source runs to see if a difference in the superheat makes the gFVar significantly different between runs. A plot of superheat vs mean gFVar in runs 193, 195, 196, 208 and 214 is shown in Figure 6.3.2. No superheat correction was deemed necessary for runs 193, 195 and 196 which were used in the gFVar discrimination analysis.

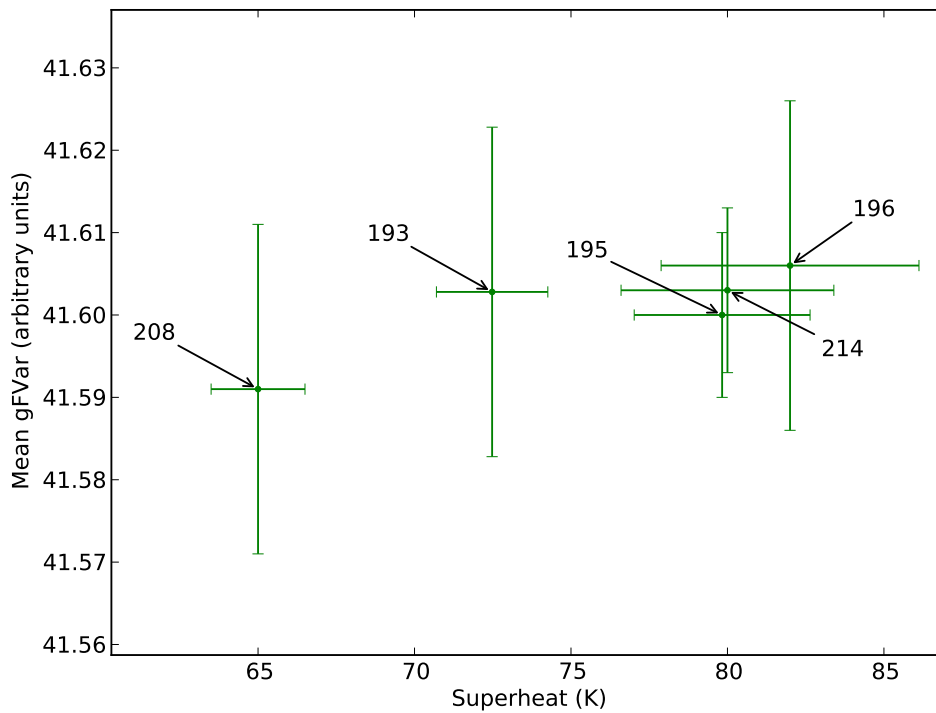


Figure 6.3.2.: Superheat vs gFVar of neutron runs 193 (6h15m), 195 (4h), 196 (3h13m) and runs with new source position 208 (3h 16m) and 214 (1h 15m)

The DFTs show no discrimination at frequencies below 10 kHz, but above 30 kHz frequencies there is strong discrimination. The gFVar variable was chosen to use the discrimination from the DFTs presented in Figure 6.3.1.

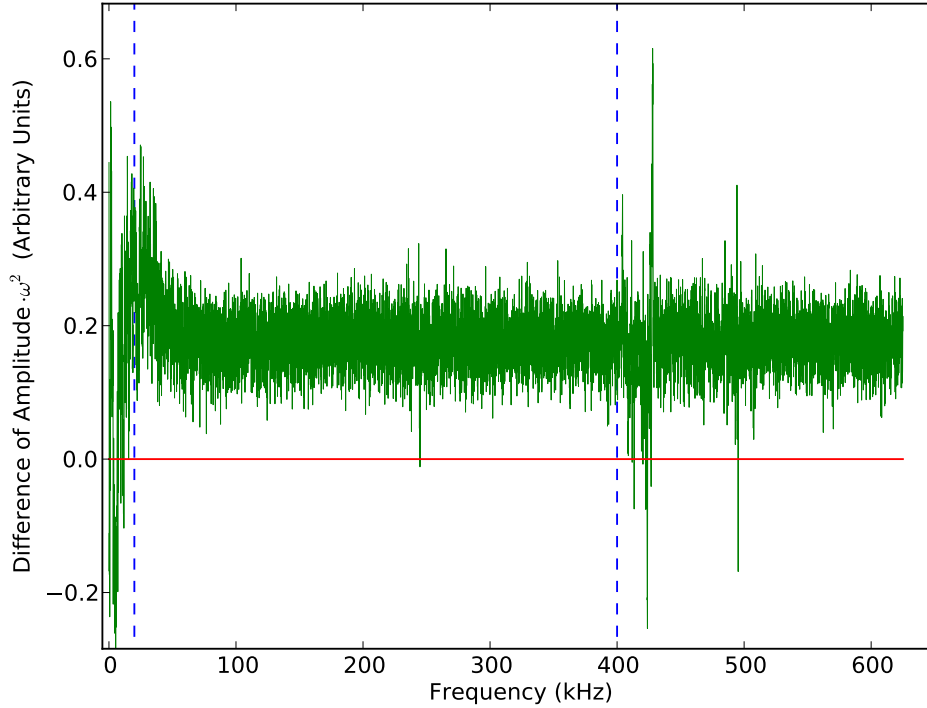


Figure 6.3.3.: The difference of average scaled DFTs between source run events and alpha run events

Mathematically, gFVar can be represented by:

$$\text{gFVar} = \sum_{20\text{kHz}}^{400\text{kHz}} A(f) \times \omega^2 \quad (6.3.1)$$

where $A(f)$ is the DFT amplitude of a given frequency window and f is the frequency. The lower bound was chosen at 20 kHz, based on Figure 6.3.3, showing the lower range of the DFT. An upper limit was chosen at 400 kHz. The distribution of gFVar in the geyser is shown in Figure 6.3.4.

An improved discrimination is seen in gFvar compared to PVar. The

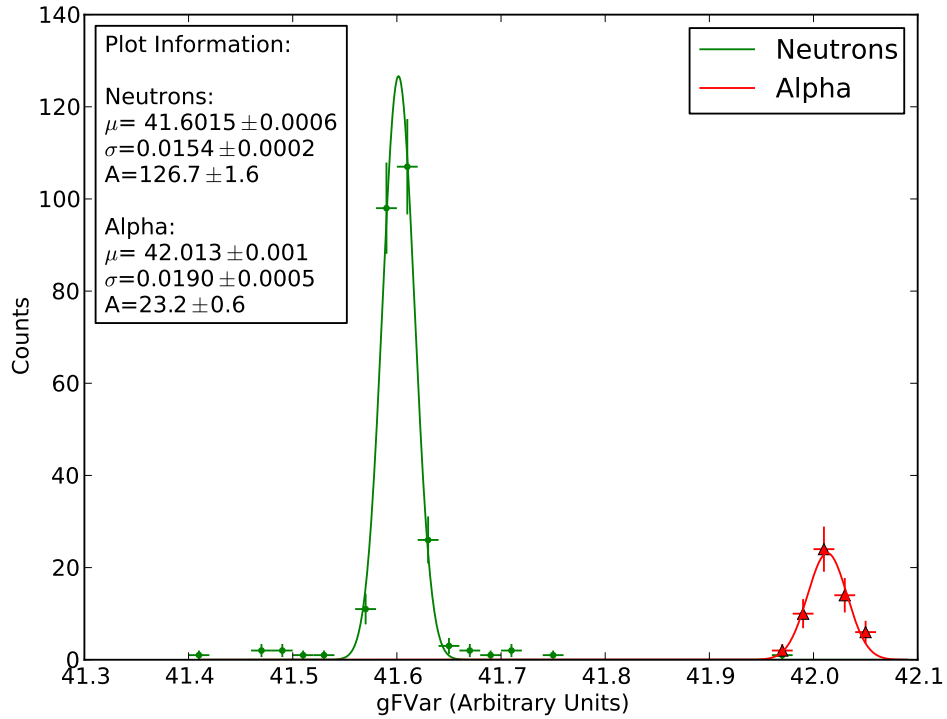


Figure 6.3.4.: Average FFT spectrum of neutrons vs alpha runs

number of events which lie in the alpha region from the neutron region is 2 ± 1 . It could be speculated that these events are multiple neutron interactions, where one neutron causes multiple nucleations. The COUPP collaboration has observed these events to have a larger acoustic emission [38]. With the data collected, a very good separation has been observed between alpha and neutrons. A tail consisting of $\sim 4\%$ of events of the neutron runs can be observed, but with the available data, no model for this background could be determined.

6.4. Expectation and Event Rates

The expected rates for the geysers are calculated assuming secular equilibrium of two of Thorium and Uranium. Secular equilibrium is the condition where the quantity of a radioactive isotope remains in equilibrium with the progenitor with the longest half life since its production rate is equal to its decay rate. Mathematically this condition is satisfied by:

$$N_B = \frac{\tau_B}{\tau_A} N_A \quad (6.4.1)$$

where N_A is the number of nuclei of any element in the chain, and τ_A is the half life of the element. In secular equilibrium, if the half life of the daughter nuclei is much less than the half life of the parent nucleus, then the activity (A) remains the same in the entire chain. Mathematically $A = N_i \lambda_i$, where i is an element in the decay chain. The activity of certain elements from the chain were measured with a Canberra HP germanium detector. Table 6.1 and Table 6.2 summarizes the rates in each chain of the reaction from the germanium counter data.

Since the decay chain is under secular equilibrium, it is expected that the activity is the same throughout the chain. However as seen in Table 6.1 a rate change is found in the 3rd row, from Bi to Pb. This indicates that the glass has a source of Bi or ²¹²Pb impurities which were introduced in the glass at the time of manufacturing or glassblowing. Table 6.2 shows the expectations

6.4 Expectation and Event Rates

Decay chain	Number of alphas	Activity from γ counting (Bq)	Total Activity (Bq)
$^{232}\text{Th} \rightarrow ^{228}\text{Ra} \rightarrow ^{228}\text{Ac} \rightarrow ^{228}\text{Th}$	1	0.213 ± 0.009	0.213 ± 0.009
$^{228}\text{Th} \rightarrow ^{224}\text{Ra} \rightarrow ^{220}\text{Rn} \rightarrow ^{216}\text{Po} \rightarrow ^{212}\text{Pb} \rightarrow ^{212}\text{Bi}$	4	0.191 ± 0.006	0.76 ± 0.02
$^{212}\text{Bi} \rightarrow ^{208}\text{Tl} \rightarrow ^{208}\text{Pb}$ or $^{212}\text{Bi} \rightarrow ^{212}\text{Po} \rightarrow ^{208}\text{Pb}$	1	1.3 ± 0.1	1.3 ± 0.1
Total	6		2.3 ± 0.1

Table 6.1.: Activity in the geyser glass vessel produced from Thorium decay chain.

from the Uranium decay chain. In this table, the activity drops in the 3rd row which may be explained by Rn created in the chain (see row 2) escaping as a gas.

Decay Chain	Number of alphas	Activity from γ counting	Total Activity
$^{238}\text{U} \rightarrow ^{234}\text{Th} \rightarrow ^{234m}\text{Pa} \rightarrow ^{234}\text{U}$	1	0.9 ± 0.3	0.9 ± 0.3
$^{234}\text{U} \rightarrow ^{230}\text{Th} \rightarrow ^{226}\text{Ra} \rightarrow ^{222}\text{Rn} \rightarrow ^{218}\text{Po} \rightarrow ^{214}\text{Pb} \rightarrow ^{214}\text{Bi}$	5	0.7 ± 0.1	3.5 ± 0.5
$^{214}\text{Bi} \rightarrow ^{214}\text{Po} \rightarrow ^{210}\text{Pb}$ or $^{214}\text{Bi} \rightarrow ^{210}\text{Tl} \rightarrow ^{210}\text{Pb}$	1	0.195 ± 0.005	0.195 ± 0.005
$^{210}\text{Pb} \rightarrow ^{206}\text{Hg} \rightarrow ^{206}\text{Tl} \rightarrow ^{206}\text{Pb}$ or $^{210}\text{Pb} \rightarrow ^{210}\text{Bi} \rightarrow ^{206}\text{Tl} \rightarrow ^{206}\text{Pb}$ or $^{210}\text{Pb} \rightarrow ^{210}\text{Bi} \rightarrow ^{210}\text{Po} \rightarrow ^{206}\text{Pb}$	1	0.195 ± 0.005	0.195 ± 0.005
Total	8		4.8 ± 0.8

Table 6.2.: Activity in the geyser glass vessel from Uranium decay chain

The total activity from the two tables is 7.1 ± 0.9 Bq. The range for 5 MeV alpha particles in glass is $\sim 24 \mu\text{m}$. The volume of the geyser with heavy

impurities that creates alpha particles is 0.482 cc with an exposure of 1.007 g compared to the total weight of 149 g. Hence, the surface activity expected in the geyser is $(7.1 \pm 0.9) \times \frac{1.007}{149}$ Bq = 0.048 ± 0.006 Bq. However, the observed surface rate in the geyser during alpha runs is 3 ± 1 events per hour or 0.0008 ± 0.0002 Bq. Hence, the alpha efficiency of the geyser is $1.6 \pm 0.7\%$.

Considering now the neutron runs, one may obtain the efficiency via the following calculation. The solid angle subtended by the source on the geyser is $\Omega = 2\pi(1 - \cos\theta)$, where theta is the angle between the line joining the source with the centre of the geyser and the line tangent on the geyser from the source. Then $\cos\theta$ is the the ratio of these 2 lines as shown in Figure 6.4.1. Considering that the source is 36 cm away from the geyser, the solid angle is $2\pi(0.00345)$ steradians. The source has an activity of $\sim 150 \pm 15$ neutrons/s, and is omnidirectional. Hence, the number of neutrons expected in the geyser is $150 \times 2\pi(0.00619)/4\pi = 0.259$ Bq. The observed neutron rate from the neutron runs is 0.006 Bq, providing a neutron efficiency of $2.3 \pm 0.2\%$.

In the geyser analysis only the bulk events are chosen. Hence, most of the alpha events come from the Radon chain. A measurement of the Radon by the geyser was made in an emanation chamber and the rate was found to have an upper limit of 2 radon nuclei per hour. Since the Radon chain gives off 4 alpha particles, the rate of events from Radon from the glass is less than 8 events per hour. The observed bulk event rate was 1.6 events per hour. Hence, the Radon efficiency of the geyser is greater than 20%.

The overall efficiency of the geyser is very low. A possible explanation for this is discussed in subsection 6.4.2. An improvement that could be made

is to perform a GEANT4 monte-carlo of the entire system in future.

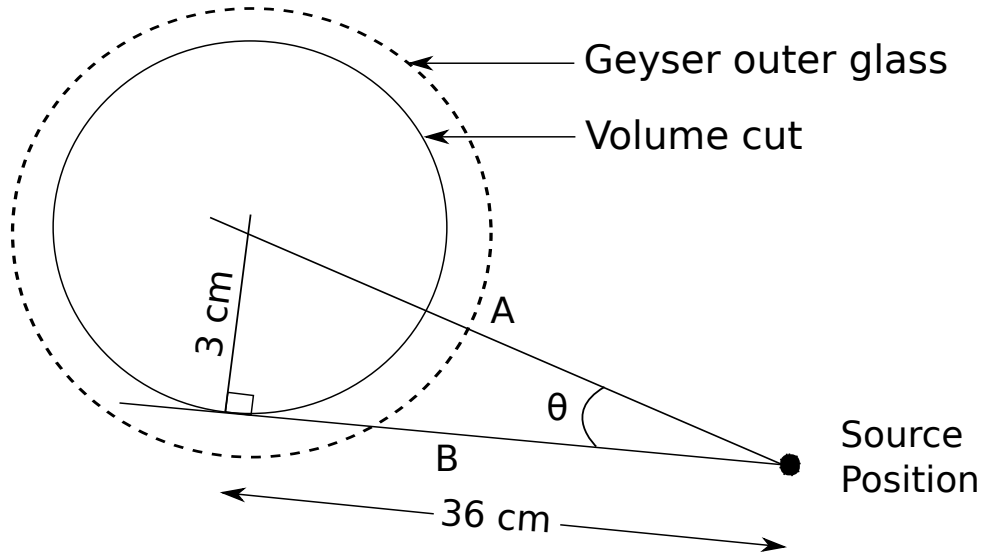


Figure 6.4.1.: Sketch of the angle measurement for source position and efficiency calculation

6.4.1. Determination of the Dead Time of the Geyser

In subsection 5.1.3 the dead time of the geyser was extracted using thermodynamic properties. The time distribution of the events in the detector contains information about the dead time as well. Here, data for two runs at 108°C and 110°C was analysed. For stochastically distributed events it is expected that the probability of events occurring drops exponentially with increasing time between events. A shortfall from this expectation at small time differences allows an extraction of the dead time. Figure 6.4.2 shows that above $\sim 120\text{s}$ the data follows the expected exponential decay, but below 120s a significant percentage of events is missing. This is consistent with the behavior observed

before in the temperature data. The dead time measurements should be taken into consideration when the efficiency of the geysler is determined.

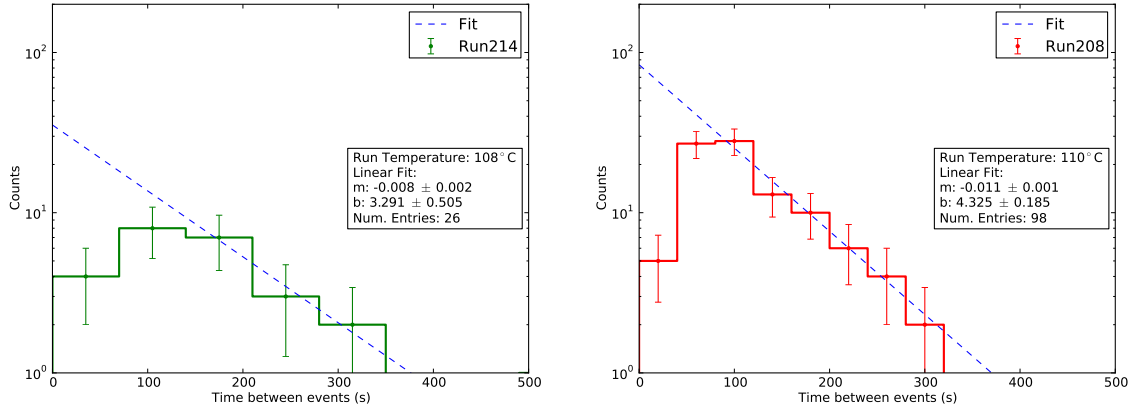


Figure 6.4.2.: Dead time measurements of runs at 108°C and 110 °C. The first two bins were not included in the fit in both plots.

6.4.2. Track Length Effects and Efficiency

Ethanol was used in this geysler, since it is economically efficient considering at this stage of the experiment where the geometry, glass-to-metal seals, heating and cooling had to be designed and commissioned. However, ethanol is a poor liquid choice in terms of particle detection with a low density and thus track lengths for 10 keV H-recoil of about 300 nm and carbon and oxygen recoils of ~250 nm as calculated by SRIM/TRIM (see: Figure 6.4.3). Hence the energy deposited by a recoil in ethanol is spread out over a distance of 300 nm. To create a protobubble, the same energy needs to be deposited within 50 nm, the typical protobubble radius. The energy density of a recoil track in ethanol is lower compared to what is required to form a bubble. This is the primary

reason for the low efficiency of the geyser. Fluorocarbons are the best fluids for bubble chambers in this regard, with higher they are density and recoil track lengths in Freons that are small. The energy density is much higher than ethanol, and closer to the required amount to form a protobubble.

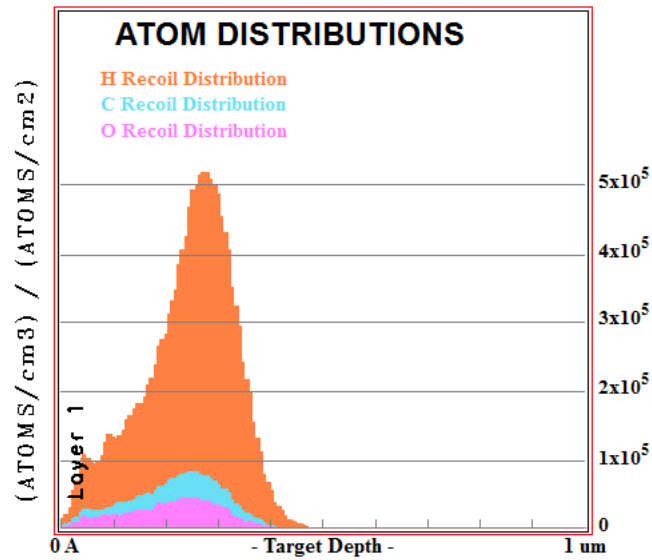


Figure 6.4.3.: Distribution of the track length generated by a SRIM simulation of 10keV recoils in ethanol.

7. Summary and Future Work

7.1. Summary and Concluding Remarks

The geometry of the prototype geyser presents stability in the operation and thermal gradient. The cooling chambers are separated by the smaller tubes of 2.5 cm length with a gradient of 40° C possible between 2 larger cooling chambers. It is possible to achieve a stable reverse gradient where the temperature of the main volume is 80 degrees above the temperature at the top. The prototype geyser has also shown that it is possible to control the temperature of the geyser to an accuracy of 1° C or less and a pressure of 0.021 bar (0.30 PSIA) or less. The cleaning procedure is satisfactory and the wall nucleation is controlled when ethanol is used as the active liquid.

The geyser was operated stably for more than 73 hours, out of which 30 hours of thermodynamic, acoustic and imaging data was analyzed. This shows that the geyser's operation is stable.

Alcohol was shown to have a discrimination effect between alpha like events and nuclear recoil like events using PVar and gFVar.

The efficiency of alcohol is very poor, and as such it is not a good fluid for particle detection. The cause of this effect is understood. Recoil track lengths in alcohol are much larger than the protobubble size, giving rise to this effect.

7.2. Freon Based Geysers

Experience has been acquired from the construction and operation of the geysers prototype which will aid in the construction of a detector with a larger active mass. Future versions of the geysers would have a much better efficiency if filled with freon since the boiling point is low, it is easier to maintain a higher superheat and the detection efficiency is much higher using freon with positioning in the pressure sensors. The prototype has shown improvements are possible in the acoustic response of the geysers and by the use of newer piezoelectric sensors with better coupling materials will permit improved data to be taken with a Freon based geysers. The challenge of a freon-based geysers will be the surface properties of the geysers vessel.

7.3. Structural Changes

7.3.1. Scale of the Experiment

The goal of the geysers experiment is to build a ton scale detector. At this scale several issues must be addressed, including a cooling tower appropriate for the scale, heating, cooling systems, enclosure and a source holder. It would

also require shielding from neutrons at a location deep underground such as SNOLAB.

7.3.2. Geyser Material

A ton scale geyser made of glass poses significant challenges of construction, handling and cleaning. Aqua-regia, used to clean the prototype geyser, is a highly corrosive acid and an industrial scale cleaning apparatus is needed to handle the quantity required to clean a ton scale geyser. An acrylic geyser is possible, but research needs to be performed on smoothness of an acrylic geyser vessel and its cleanliness.

7.3.3. Liquid Level Control

For a geyser to be stable, the transport of liquids across different temperatures of the condensation chamber must be kept at a minimum. This is achieved by controlling the size of the bubble. The empty space at the top of the geyser's cooling chamber controls the size of the bubble, and hence it is crucial to control the top space. A liquid level control needs to be designed and built. The geyser will become much more stable, and will have a reduced dead time once the volume at the top is adequately controlled.

7.3.4. Retroreflectors and Diffuse Lighting

In the present geyser, the optical data analysis was made challenging by the fact that the camera and the light source were not positioned optimally. In a future geyser a retroreflector could be used in conjunction with diffuse lighting. A faster camera system would also improve the optical data acquisition.

7.4. Data Acquisition Upgrade

The pressure transducer presently collects data at 10Hz. This is too slow to observe the pressure rise when a bubble forms and to distinguish bulk events from wall events as done by COUPP.

Bibliography

- [1] JH Jeans. The Motions of the Stars in a Kapteyn Universe. *Monthly Notices Roy. Astron. Soc.*, 82:122, 1922.
- [2] F. Zwicky. Die Rotverschiebung von extragalaktischen Nebeln. *Helvetica Physica Acta*, 6:110–127, 1933.
- [3] Richard Massey, Jason Rhodes, Richard Ellis, Nick Scoville, Alexie Leauthaud, Alexis Finoguenov, Peter Capak, David Bacon, Hervé Aussel, Jean-Paul Kneib, Anton Koekemoer, Henry McCracken, Bahram Mobasher, Sandrine Pires, Alexandre Refregier, Shunji Sasaki, Jean-Luc Starck, Yoshi Taniguchi, Andy Taylor, and James Taylor. Dark matter maps reveal cosmic scaffolding. *Nature*, 445(7125):286–90, January 2007.
- [4] N. Jarosik, C. L. Bennett, J. Dunkley, B. Gold, M. R. Greason, M. Halpern, R. S. Hill, G. Hinshaw, A. Kogut, E. Komatsu, D. Larson, M. Limon, S. S. Meyer, M. R. Nolta, N. Odegard, L. Page, K. M. Smith, D. N. Spergel, G. S. Tucker, J. L. Weiland, E. Wollack, and E. L. Wright. Seven-Year Wilkinson Microwave Anisotropy Probe (WMAP) Observa-

- tions: Sky Maps, Systematic Errors, and Basic Results. *Astrophysical Journal Supplement Series*, page 42, January 2010.
- [5] Barbara Ryden. *Introduction to cosmology*. Addison-Wesley, San Francisco, 2003.
- [6] James Schombert. Lecture 17, Dark Matter/Energy.
- [7] V. C. Rubin, N. Thonnard, and W. K. Ford. Extended rotation curves of high-luminosity spiral galaxies. IV - Systematic dynamical properties, SA through SC. *The Astrophysical Journal*, 225:L107, November 1978.
- [8] John T. Stocke, J. Michael Shull, and Steven V. Penton. The Baryon Content of the Local Intergalactic Medium. page 25, July 2004.
- [9] M. Milgrom. A modification of the Newtonian dynamics as a possible alternative to the hidden mass hypothesis. *The Astrophysical Journal*, 270:365, July 1983.
- [10] Jacob Bekenstein. Relativistic gravitation theory for the modified Newtonian dynamics paradigm. *Physical Review D*, 70(8):083509, October 2004.
- [11] Maruša Bradač, Steven W. Allen, Tommaso Treu, Harald Ebeling, Richard Massey, R. Glenn Morris, Anja von der Linden, and Douglas Applegate. Revealing the Properties of Dark Matter in the Merging Cluster MACS J0025.4-1222. *The Astrophysical Journal*, 687(2):959–967, November 2008.
- [12] Stephen Serjeant. *Observational Cosmology*. Cambridge University Press, 2010.

- [13] Kris Sigurdson, Michael Doran, Andriy Kurylov, Robert Caldwell, and Marc Kamionkowski. Dark-matter electric and magnetic dipole moments. *Physical Review D*, 70(8):083501, October 2004.
- [14] F S Ling, E Nezri, E Athanassoula, and R Teyssier. Dark matter direct detection signals inferred from a cosmological N-body simulation with baryons. *Journal of Cosmology and Astroparticle Physics*, (1002):012, February 2010.
- [15] Annika H. G. Peter and Andrew J. Benson. Dark-matter decays and Milky Way satellite galaxies. *Physical Review D*, 82(12):123521, December 2010.
- [16] Frederick Seitz. On the Theory of the Bubble Chamber. *Physics of Fluids*, 1(1):2, January 1958.
- [17] Paul Dergarabedian. *The rate of growth of vapor bubbles in superheated water*. Doctoral thesis, Caltech, March 1952.
- [18] Stanley Alan Zwick. *The growth and collapse of cavitation bubbles*. Doctoral thesis, Caltech, January 1955.
- [19] M. Barnabé-Heider, M. Di Marco, P. Doane, M.-H. Genest, R. Gornea, R. Guénette, C. Leroy, L. Lessard, J.-P. Martin, U. Wichoski, V. Zacek, K. Clark, C.B. Krauss, A.J. Noble, E. Behnke, W. Feighery, I. Levine, C. Muthusi, S. Kanagalingam, and R. Noulty. Response of superheated droplet detectors of the PICASSO dark matter search experiment. *Nuclear Instruments and Methods in Physics Research Section A: Accelerators, Spectrometers, Detectors and Associated Equipment*, 555(1-2):184–204, December 2005.

- [20] Milton Blander and Joseph L. Katz. Bubble nucleation in liquids. *AICHE Journal*, 21(5):833–848, September 1975.
- [21] C. T. Avedisian. The Homogeneous Nucleation Limits of Liquids. *Journal of Physical and Chemical Reference Data*, 14(3):695, July 1985.
- [22] Robert Cole. *Advances in Heat Transfer Volume 10*, volume 10 of *Advances in Heat Transfer*. Elsevier, 1974.
- [23] S. Archambault, F. Aubin, M. Auger, E. Behnke, B. Beltran, K. Clark, X. Dai, A. Davour, J. Farine, R. Faust, M.-H. Genest, G. Giroux, R. Gornea, C. Krauss, S. Kumaratunga, I. Lawson, C. Leroy, L. Lessard, C. Levy, I. Levine, R. MacDonald, J.-P. Martin, P. Nadeau, A. Noble, M.-C. Piro, S. Pospisil, T. Shepherd, N. Starinski, I. Stekl, C. Storey, U. Wichoski, and V. Zacek. Dark matter spin-dependent limits for WIMP interactions on ^{19}F by PICASSO. *Physics Letters B*, 682(2):185–192, November 2009.
- [24] Pitam Mitra. Calculations for Bubble Size and Volume Ratio and Feasibility of the Geysers. Technical report, PICASSO Scientific and Technical Reports PSTR 11-004, 2011.
- [25] L D Landau and E.M. Lifshitz. *Fluid Mechanics, Second Edition: Volume 6 (Course of Theoretical Physics)*. Butterworth-Heinemann, 1987.
- [26] M. Minnaert. XVI. On musical air-bubbles and the sounds of running water. *Philosophical Magazine Series 7*, 16(104):235–248, 1933.
- [27] Connie Storey. *The Development of an Event Localization Algorithm for*

- the PICASSO Dark Matter Experiment*. Masters thesis, Queen's University, 2007.
- [28] F Aubin, M Auger, M-H Genest, G Giroux, R Gornea, R Faust, C Leroy, L Lessard, J-P Martin, T Morlat, M-C Piro, N Starinski, V Zacek, B Beltran, C B Krauss, E Behnke, I Levine, T Shepherd, P Nadeau, U Wichoski, S Pospisil, I Stekl, J Sodomka, K Clark, X Dai, A Davour, C Levy, A J Noble, and C Storey. Discrimination of nuclear recoils from alpha particles with superheated liquids. *New Journal of Physics*, 10(10):103017, October 2008.
- [29] Michael Browne. *Preparation for Deployment of the Neutral Current Detectors (NCDs) for the Sudbury Neutrino Observatory*. Doctoral thesis, North Carolina State University, 1999.
- [30] D.-M. Mei and A. Hime. Muon-induced background study for underground laboratories. *Physical Review D*, 73(5):053004, March 2006.
- [31] V Zacek. PICASSO+ LOI. Technical report, SNOLAB, 2012.
- [32] C Antoine. Tensions des vapeurs; nouvelle relation entre les tensions et les températures. *Comptes Rendus des Séances de l'Académie des Sciences. Paris.*, 107:681–684, 778–780, 836–837, 1888.
- [33] B. Hahn and H.W. Reist. The Geyser, a new detector for nuclear recoils. In *High Energy Physics and Nuclear Structure*, pages 432–435, 1973.
- [34] Twisted Matrix Labs. Twisted [Computer Software] Available from: twistedmatrix.com.

- [35] GHP Cohen and GA Coon. Theoretical consideration of retarded control. *Trans. Asme*, 75(1):827–834, 1953.
- [36] Pitam Mitra. AutoGeysler [Computer Program] available from github.com/xtachx, 2012.
- [37] K Klassen. Galileo Solid-State Imaging Subsystem Calibration Report: Part 2. Technical report, JPL - D5880, 1993.
- [38] E. Behnke, J. Behnke, S. J. Brice, D. Broemmelsiek, J. I. Collar, A. Conner, P. S. Cooper, M. Crisler, C. E. Dahl, D. Fustin, E. Grace, J. Hall, M. Hu, I. Levine, W. H. Lippincott, T. Moan, T. Nania, E. Ramberg, A. E. Robinson, A. Sonnenschein, M. Szydagis, and E. Vázquez-Jáuregui. First dark matter search results from a 4-kg CF-₃I bubble chamber operated in a deep underground site. *Physical Review D*, 86(5):052001, September 2012.

A. Appendix

A.1. Runs Considered for Analysis

Date	Run Number	Type	Temperature (°C)	Pressure (PSI)	Duration
11-21-2012	193	Neutron	107.2 ± 0.2	$2.3 \pm .2$	6h 15m
11-22-2012	195	Neutron	107.3 ± 0.2	$1.6 \pm .2$	4h 0m
11-23-2012	196	Neutron	107.4 ± 0.2	$1.4 \pm .3$	3h 13m
12-07-2012	201	Alpha	107.9 ± 0.2	$3.0 \pm .2$	7h 33m
12-17-2012	204	Alpha	108.0 ± 0.1	$2.2 \pm .2$	7h 30m
12-21-2012	205	Alpha	107.8 ± 0.2	$2.1 \pm .1$	4h 50m
12-24-2012	206	Alpha	107.7 ± 0.2	$2.2 \pm .1$	2h 9m
02-07-2013	208	Neutron	107.2 ± 0.2	$3.4 \pm .2$	3h 16m
02-08-2013	211	Neutron	111.9 ± 0.2	$4.4 \pm .3$	1h
02-14-2013	214	Neutron	105.5 ± 0.2	$1.4 \pm .3$	1h 15m

Table A.1.: Runs considered for analysis. Runs 195 and 196 have a lower pressure because the vacuum pump was used to degas the geyser prior to running. In run 201, a peltier cell was nonfunctional due to a water leak in the cooling loop.

A.2. Contents of a .wfi file

- Number of bytes: The total number of bytes in the trigger. Since each sample is 2 bytes, this would be 100000 for each sampling window.
- Vertical gain: Multiplication factor to convert ADC values to voltage. A typical value will be around 10^{-6} V / ADC units
- Vertical offset: Offset in Volts.
- Horizontal interval: Gives the time interval between each sample. For a frequency of 1.25Mhz, this should be 8×10^{-7} s/bin.
- Horizontal offset: The offset with respect to the signal's zero-position on the x-axis for the signal.
- Number of traces: Number of traces in the data file. In the DAQ system, we have 1 trace per file.
- Number of bytes per data-point: 2 bytes per data point.
- Keep all datapoints: Old LeCroy scopes used this to record missing data points. A new Tektronix scope was used for this experiment, so this doesn't apply.